# Frequency Scatter in Kinetic Inductance Detectors: Improved Analysis Using Pixel-to-Frequency Mapping Setup

Bachelor Thesis

Gabriël Lomans

Delft University of Technology

TU Delft

# Frequency Scatter in Kinetic Inductance Detectors: Improved Analysis Using Pixel-to-Frequency Mapping Setup

by

G.J. Lomans

to obtain the degree of Bachelor of Science in Applied Physics at the Delft University of Technology.

| | |
|---|---|
| Academic year: | 2023/2024 |
| Student number: | 5252563 |
| Date of defense: | 17 November 2023 |

| | |
|---|---|
| Thesis Committee: | Prof.dr.ir. J.J.A. (Jochem) Baselmans[1,2] |
| | Dr. A.J.L. (Aurèle) Adam[3] |
| Daily Supervisor: | Ir. W.G. (Wilbert) Ras[1,2] |
| Study Program: | BSc Applied Physics |
| Faculty: | Applied Sciences |

[1]*SRON Netherlands Institute for Space Research, Niels Bohrweg 4, 2333 CA Leiden, Netherlands*
[2]*Faculty of Electrical Engineering, Mathematics and Computer Science, Delft University of Technology, Mekelweg 4, Delft 2628 CD, Delft*
[3]*Faculty of Applied Sciences, Delft University of Technology, Department of Imaging Science and Technology, Lorentzweg 1, 2628 CJ Delft, Netherlands*

Cover: An image of the $45 \times 45$ spatial map, which was created based on measurements of the $20 \times 20$ KID array. Each pixel represent a single KID, where the color is an indication of their respective operating frequency.

# Abstract

Extremely large telescopes (ELTs) are expected to be one of the most promising astronomical observation instruments when it comes to observing exoplanets. During observations, however, Earth's atmosphere introduces optical distortion, which needs to be corrected. For this reason, a wavefront sensor (WFS) will be developed that comprises a $100 \times 100$ array of kinetic inductance detectors (KID), superconductor-based photodetectors. The main advantage of KIDs in an array is their ability to be multiplexed on a single read out line by designing each KID to operate at a different frequency. The signal of an individual KID can essentially be described as a dip in the transmission signal of the readout signal. Upon the fabrication of these KID arrays, however, these dips may have shifted as so-called frequency scatter (or f-scatter), which severely disorders the readout signal. The f-scatter cannot be determined based solely on the readout signal as it contains no information about which KID each individual signal originates from.

This paper manages to provide a solution in the form of an experimental method in which the KID array is scanned along the x- and y-axis to produce a spatial map. To realize this, an optical setup was designed and constructed, based on a single-lens system with a magnification of $M = -1.22$. By implementing a CCD camera, the KID array could be live imaged to align the setup accordingly. Thanks to numerous other alignment measures, the setup was able to scan the entire KID array along the x- and y-axis in 45 scans per axis. Based on the difference in transmission, a $45 \times 45$ spatial map was constructed, which was manually scaled down to $20 \times 20$. This $20 \times 20$ spatial map presented the location of KIDs on the fabricated detector array based on their measured operating frequency. By comparing this with the spatial map of the KID array design, the standard deviation in the fractional frequency deviation was determined, $\sigma_{\delta f/f} = 5.92 \cdot 10^{-3}$. This result shows the experimental method is able to effectively unveil the severity of the f-scatter in the studied $20 \times 20$ KID array.

Despite the potency of the presented method, the biggest giveaway of its flaws is a reduced pixel yield on the $20 \times 20$ spatial map from 400 to 374 pixels. The developed data analysis is able recognize multiple complications, which can be mitigated by optimizing readout parameters to improve the quality of the signal. Additionally, one-to-one imaging is far too restricting for advanced scanning techniques due to its fixed $M$. Appropriate suggestions for improving the lens systems would be implementing the Cooke triplet or a two-lens system that utilizes the principle of virtual imaging.

# Acknowledgements

Over the course of two intense months, I have delved into the intricacies of kinetic inductance detectors. Embarking on the journey that was my bachelor thesis project has been an enriching experience for me and I could not have wanted it any other way. Beyond the academic growth I have undergone, I am able to recognize and appreciate my personal and intellectual development. This wonderful opportunity I have been given allowed me to discover a million ways to fall, but also a million ways to get back on my feet. This could not have been possible without the following people, whom I would like to express my sincerest gratitude to.

My daily supervisor Ir. W.G. Ras for his tireless assistance, inspiring words of motivation and comforting support in some of my most trying times. My thesis committee members, Prof.dr.ir. J.J.A. Baselmans and Dr. A.J.L. Adam, for dedicating their time to read and evaluate my thesis. Dr. P.J. de Visser, for lending a helping hand in the design and construction of the setup and for providing me with feedback on this thesis. K. Kouwenhoven for designing the detectors, showing me around the cleanroom and providing me with insightful details about the measurement procedure.
My wheel-gymnastics coaches and team members, for creating a safe space for me to release my stress in one of the most special art forms I know. The friends I made throughout my bachelor program at the TU Delft and Seoul National University, for accepting me into their lives for who I am. Finally, I would like to thank my family on both sides of the Atlantic Ocean, for their strength and unconditional warmth since the very first day I opened my eyes to the world.

"If one thing had been different, would everything be different today?"
*Dr. Taylor Alison Swift, 2020*

# Contents

# Chapter 1

# Introduction

The desire to acquire more knowledge about the world outside the earth's atmosphere and even beyond the solar system, has been around for centuries. Throughout its lifetime, mankind has developed technologies that has lead to deeper insights of the universe, one more revolutionary than the previous. One of the biggest questions that has occupied the human mind up to this very moment is: "are we alone in the universe?" Until recently, finding an answer has never seemed so probable, as the existence of exoplanets within the habitable zone around their respective star could provide information that will lead to one.

Currently, extremely large telescopes (ELTs) are being developed to serve the very purpose of studying these exoplanets. These devices are equipped with over 30 mirrors nowadays in order to realize the detection and characterization of rocky planets around smaller red stars. However, the Earth's atmosphere introduces significant wavefront distortion into measurements. To achieve full sensitivity and angular resolution of the ELTs, these distortions need to be corrected. Such a correction can be done through the implementation of a wavefront sensor (WFS). The development of a WFS for this specific application involves kinetic inductance detectors (KIDs), a superconductor-based photodetector. What makes KIDs so suitable as photodetectors is the absence dark current, which means the detector will not produce a response when there is no photon detection. Additionally, KIDs have no read noise, have the ability to resolve chromatic wavefront distortions, and can be operated at high speeds without lowering the SNR. [1] [2]
Compared to conventional semiconductor-based photodetectors, KIDs are easier in facilitating frequency division multiplexing (FDM). By designing each KID in an array to operate at a particular frequency $f_0$, the KIDs can be multiplexed on a single readout line, which significantly reduces the amount of required electronic readout components for a single WFS. In the design for such a KID array, the operating frequencies are uniformly dispersed across a decided frequency band, a consistent frequency spacing $\phi$. However, the fabrication of these KIDs is likely to deliver different operating frequencies than what the design intended, $f_0 + f$. This shift in operating frequency across the KID array is referred to as frequency scatter or f-scatter. The resulting readout signal presents a disordered arrangement of individual KID responses. While reorganizing seems straight forward, the readout signal does not have any information ingrained about which response originates from which KID on the detector array. This makes it impossible to determine the f-scatter across a KID array.

The main objective of this paper is to design and test an experimental method to inspect the f-scatter in a $20 \times 20$ KID array. The principle of this method is performing a scan on the fabricated detector array along the x- and y-axis to produce a spatial map. Chapter 4 will go over the entire design and construction process of an optical system, crucial for the scanning procedure. As this involves a large understanding of geometrical optics and the branch of aberration optics, an entire chapter is dedicated to discussing the optical system completely. An elaborate overview of several setup components and their role in the measurement procedure is displayed in chapter 5. This chapter also touches on the data analysis architecture, developed to interpret the obtained measurements. Chapter 6 presents a thorough analysis of the $20 \times 20$ KID array, as

well as the findings from the spatial maps comparison. Lastly, a summary and thorough evaluation of the experimental method development is given in chapter 7.

# Chapter 2

# Physical Principle of the KID

## 2.1 Superconductivity

When looking at the electromagnetic spectrum, of which a chart is available in Appendix A, the visible optical photons range in wavelength from $\lambda = 400-700$ nm, which is inversely related to their frequency $f$ and their energy $E$. This feature of visible light is exploited in current optical instruments through the implementation of superconductor technology. Superconductivity is characterized as a complete conductive state where electrons can travel through the lattice of a solid with zero electrical resistance and exclusion of magnetic field effects. This conductive state can only be achieved below a critical temperature $T_c$, characteristic to the material. When this is the case, valence electrons drop down to the Fermi energy level $E_F$, bound by the Pauli exclusion principle. Simultaneously, the negatively charged valence electrons will attract positively charged particles around them, bending the lattice. These deformations will provide a slightly positively charged shield for the valence electrons, labeled as phonons. Due to the critically low temperatures $T < T_c$, the electron-phonon interaction is able to overcome the Coulomb repulsion between two electrons, causing two valence electrons to pair up and form a new bound state. These electron pairs, referred to as Cooper pairs, behave as bosons and will therefore have the tendency to "condense" into the same energy ground state, responsible for the superconductive properties of a material. [3]
The electron-phonon interaction that Cooper pairs are subjected to is particularly weak, which is the reason this pairing only takes place at low temperatures $T < T_c$ and the resulting pairs are extremely sensitive to smallest of energy supplies. The energy of each individual electron in a Cooper pair amounts to

$$\Delta \approx 1.76 k_B T_c \tag{2.1}$$

with $k_B$ read as the Boltzmann constant and $\Delta_0$ when $T \to 0$. This means that an incident photon energy exceeding the binding energy of the Cooper pair, $h\nu > 2\Delta$, will break up the Cooper pair and give rise to the excitation of particles carrying an energy $E \geq E_F + \Delta$. These particles are labeled as quasiparticles, which can be described either as charged particles that behave as if they had a modified effective mass or as a collective behaviorism of particles that can be quantified as a single particle, or a combination of both. The quasiparticle excitations from the ground state have no states available to them within $2\Delta$ from $E_F$, an energy barrier. [3]

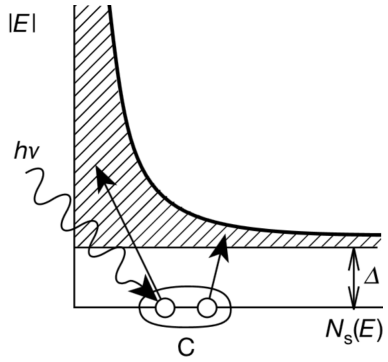


Figure 2.1: A schematic representation of the absorption of photon energy at $h\nu > 2\Delta$ by a Cooper pair. The Cooper pair in this superconducting material resides at the Fermi energy $E = E_F$, on the x-axis, before it is broken by the photon energy, resulting in the creation of two quasiparticles. [4]

While Cooper pairs split into quasiparticles, quasiparticles may recombine into Cooper pairs, which is largely dependent on the applied temperature. An increase in temperature due to impact of an energetic photon, increases the rate at which this recombination occurs called the quasiparticle recombination time,

$$\tau_{\text{qp}} = \frac{\tau_0}{\sqrt{\pi}} \left( \frac{k_B T}{2\Delta} \right)^{5/2} \sqrt{\frac{T_c}{T}} e^{\Delta/k_B T} \tag{2.2}$$

and in turn decreases the quasiparticle density $n_{\text{qp}}$ of the superconductive material

$$n_{\text{qp}} \approx 2N_0 \sqrt{2\pi k_B T \Delta} e^{\Delta/k_B T} \tag{2.3}$$

where $\tau_0$ and $N_0$ are the recombination time at $T \to 0$ and the density of singly occupied states at the Fermi level $E = E_F$ respectively. [5] Through the expressions for $n_{\text{qp}}$ an expression for the number of quasiparticles produced per incident Cooper pair-breaking photon can be described by

$$N_{\text{qp}} = n_{\text{qp}} V = \frac{\eta \tau_{\text{qp}} P_{rad}}{\Delta} = \frac{\eta h\nu}{\Delta} \tag{2.4}$$

where $\eta$ represents the pair-breaking efficiency, or the quasiparticle production efficiency, and takes on a value of $\approx 0.57$. The erratic generation and recombination of quasiparticles gives detectors utilizing superconductor technology an interesting characteristic, which will be explored in section 2.2.

## 2.2 Kinetic Inductance

The change of the number of quasiparticles in a superconductive material is accompanied by a change in conductivity of the superconductor, a relation which has been explored by Gao et al. [6]. The greater catch is that quasiparticles, contrasting with Cooper pairs, are resistive and hence introduce a resistivity within the superconductive material.

When a DC current is applied to a superconductor at $T < T_c$, it becomes perfectly conductive. The electric field present in the superconductor causes Cooper pairs to accelerate and store kinetic energy without any dissipation. However, when an AC current is applied, the superconductor has a nonzero impedance. As the AC current provides an alternating electric field near the surface of a superconductor, the Cooper pairs are accelerated in an alternating direction according to the applied current. Because the Cooper pairs have a non-zero mass, their inertia does not allow this redirection to occur instantaneously, which is reflected in a delay in the outgoing signal. The AC current therefore causes the superconductor to act like an inductor, of which the total inductance $L_{\text{tot}} = L_k + L_s$ is the sum of the kinetic inductance and the geometric impedance or the surface impedance. When a Cooper pair is broken up, the resulting quasiparticles travel through the

superconductor with a significant resistivity, leading to a change in the surface impedance of the surface impedance, which reads

$$Z_s = R_s + j\omega L_s \tag{2.5}$$

where $\omega$ represents the angular frequency of the applied alternating current and $R_s$ the surface resistance of the superconductive material. [7] Due to quasiparticle generation, the remaining Cooper pairs are accelerated in order to maintain the same current. Since the kinetic energy of a Cooper pair is related to their squared velocity, the kinetic inductance $L_k$ and, consequently, the total inductance $L_{\text{tot}}$ is increased.

## 2.3 Resonators

The change in complex surface impedance $Z_s$ of a superconducting film with thickness $d$ is what will be measured when detecting incident microwave photons. A photon with an energy $h\nu > 2\Delta$ breaking up Cooper pairs results in a reaction within the superconductor, which can be readout by embedding the superconductor as a variable inductor in a resonator circuit, displayed in figure (2.2(a)).
The reaction of parallel resonance circuits or RLC circuits, are decided by the capacitance $C$ and inductance $L$ implemented in the circuit. At resonance frequency, given by

$$f_0 = \frac{1}{2\pi\sqrt{L_{\text{tot}}C}} \tag{2.6}$$

the inductance will be such that the impedance of the entire system becomes purely resistive. The conduction of electrical current reaches a minimum at $f_0$, which can be visualized by a dip response signal of the resonator, see figure (2.2(b)). [8]
When a photon with sufficient energy hits the superconductor, the number of quasiparticles in the material $N_{\text{qp}}$ will increase. Given quasiparticles are resistive, while Cooper pairs are not, the creation of quasiparticles will be accompanied by the introduction of a resistance term in the surface impedance from equation (2.5). According to equation (2.6), the impact of a sufficiently energetic photon thus results in a negative shift in the resonance frequency $\delta f$. Along with this change, the amount of transmitted power is altered $\delta|S_{21}|$ with a positive shift. The result is a response signal that shows a dip at a frequency which is lower and more shallow than the dip was before the resistor experienced the impact of an energetic photon. These changes in the response signal of the resonator are visualized in figure (2.2(b)). [2]
A way of expressing the behavior of a resonator to a change in conductivity is the quality factor $Q$. The total quality factor of a system is a measure of how much energy is stored in the resonator circuit relative to the amount of dissipated power and is expressed.

$$Q = \frac{P_{\text{stored}}}{P_{\text{diss}}} = \frac{f_0}{\Delta f} = \frac{\omega L_{\text{tot}}}{R} \tag{2.7}$$

where $\Delta f$ is the FWHM of the resonance dip. The quality factor can be divided into the coupling power and the intrinsic power, which are related according to $Q = Q_c + Q_i$. The former term is defined as the efficiency of energy storage in the capacitive coupling between the resonator and the readout line. The latter is due to internal losses of the resonator.
As mentioned earlier in this section, one way of observing the change in the resonator response is by reading at the transmission amplitude of signal $|S_{21}|$. Provided the surface impedance is a complex expression, the transmission value $S_{21}$ becomes complex as well, which has been shown by Ras in their research on kinetic inductor detectors for MIR photons. Derivable from this complex transmission value are the transmission amplitude $|S_{21}|$ and the transmission phase $\theta$, of which the behavior according to a change in the complex surface impedance is displayed in figures (2.2(c)) and (2.2(d)).

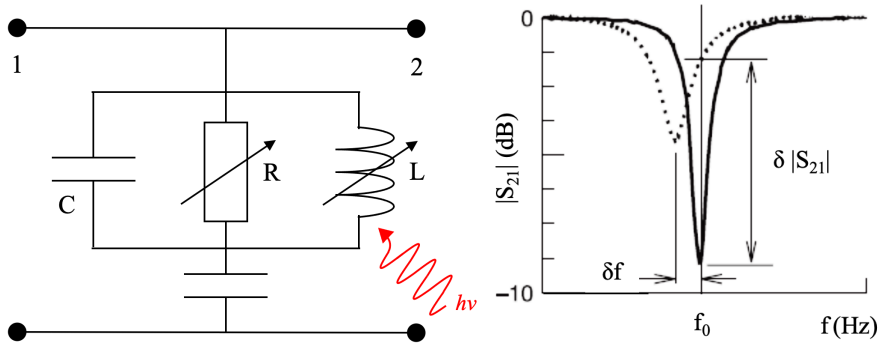


(a) RCL circuit

(b) f and $|S_{21}|$

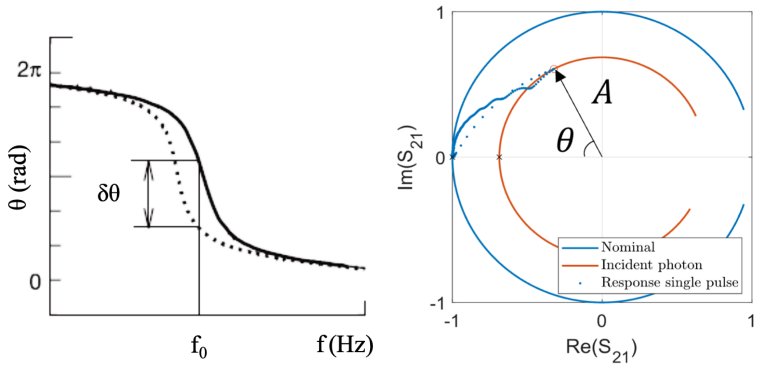


(c) f and $\theta$

(d) $|S_{21}|$ and $\theta$

Figure 2.2: Figure (**a**) shows the circuit diagram of a resonance circuit, or an RCL circuit. The inductor $L$ represents the component of the detector which detects incident photons. Figure (**b**) and (**c**) show the response signal of the RCL circuit in terms of transmission amplitude $|S_{21}|$ and phase $\theta$ respectively. The response is in the shape of a dip located at resonance frequency $f_0$ and with an amplitude of $|S_{21}|$. When the inductor absorbs energy from an incident photon, both quantities change. As the resonance frequency shifts to a lower value $\delta f$, the amplitude is much smaller $\delta|S_{21}$ and the phase increases $\delta\theta$. Additionally the dip at $f_0 + \delta f$ is less narrow that the dip at $f_0$. The change of the transmission amplitude and phase is illustrated together in a complex circle, figure (**d**), which is possible due to the fact that the transmission coefficient itself is a complex expression itself. [1] [2]

# Chapter 3

# KID Design

In this section, an overview will be presented of the design of the $20 \times 20$ optical LEKID array studied in this paper. The design of this KID array was carried out by K. Kouwenhoven [9]. A summary for the $6 \times 6$ variant, which has many similarities, can be found in the summary of the KID resolving power.
The KID components will first be discussed from an analytical point of view, followed by the fabrication of the chips. Subsequently, this section will present the concept of frequency division multiplexing, concluded by an overview of several noise sources that generally may arise in KIDs.

## 3.1 Layout

As mentioned in section 2.3, a change in the kinetic inductance due to an incident photon, can be measured by embedding a superconductive film in a resonance circuit. The design for the resonance circuit of the lumped element kinetic inductance detector (LEKID), used in this paper, is displayed in figure (3.1) alongside the electrical circuit diagram of this resonance circuit (2.2(a)).

### 3.1.1 Individual KID

Each KID has its own resonance frequency $f_0$, which is dependent on both the inductance $L$ and the capacitance $C$. The inductor of the KID used in this paper, visible in figure (3.1) shaded purple, was fabricated with the material $\beta$-Ta for its highly resistive properties. As the design demonstrates, the superconductor was implemented as a 60 nm thick film, meandering across its reserved area.
The interdigitated capacitor (IDC) represents the capacitive component in the KIDs electrical circuit, shaded white against a red background in figure (3.1). This structure is comprised of two intertwined comb-like structures. The teeth of these structures, which will be referred to as fingers, have a specific width and length and are laid out in an alternating pattern. By varying the length of the fingers, while keeping the structure of the inductor fixed, the capacitance can be altered, which in turn alters the resonance frequency according to equation (2.6). This enables easily adjustable $f_0$-values for different KID designs.
Moreover, in the production of the optical KIDs studied in paper, the material NbTiN was used for the IDC sturcture. According to Kouwenhoven et al., the chosen material benefits the confinement of quasiparticles to only the sensitive part of the detector, reducing readout noise, which will be discussed later in this section.
An aluminium bridge, shaded purple in figure (3.1), connects the IDC to the coplanar waveguide (CPW) readout-line, which runs along the IDC and is fabricated with the same material as the IDC. The CPW readout-line directs the response signal of the KID to the readout instrumentation further along.

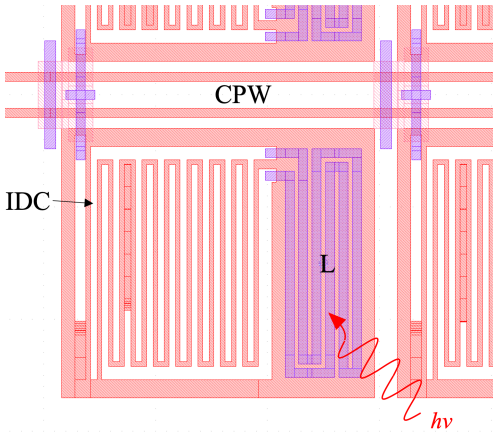


Figure 3.1: The design of a single LEKID. The inductor $L$, the photosensitive component of the RCL circuit, is shaded in purple and the IDC structure, representing the capacitive component $C$, is shaded white on a red background. One of the fingers of the IDC is trimmed to give the KID in this design its own characteristic resonance frequency $f_0$. [9]

### 3.1.2 KID Array

One of the biggest advantages of a KID is its efficiency in frequency division multiplexing, which is greatly exploited for the creation of large format detector arrays. In order to produce a signal consisting of multiple non-overlapping signals, the resonators may simply be coupled to the same readout line, as demonstrated in figure (3.2(b)). The multiplexed signal is then readout from the CPW line, reducing the amount of required readout electronics.

This paper focuses on a 3×3 mm array of 20×20 KIDs, each KID measuring 150×150 $\mu$m. The IDC geometry throughout this detector array is designed to provide for each KID an $f_0$-value from two separate frequency bands. The first frequency band, frequency band A, ranges from 4.55 to 5.35 GHz and the second, band B, from 5.65 to 6.45 GHz. Each band has non-overlapping signals spaced at $\langle\phi\rangle$ = 4 MHz with negligible deviation according to the design. This is achieved by cutting the finger length of each subsequent KID shorter in consistent increments. These increments range from 0.5 to 1.73 nm and have been decided upon based on the theoretical $f_0$ the resonator would yield, with greater finger cut increments in the lower $f_0$ region and smaller finger cut increments as the $f_0$ values increase.

On top of the KID array rests an array of micro-lenses made of fused silica, which purpose is to converge incident light bundles onto the inductor of the individual KIDs. Each micro-lens has a base of 150 ± 1 $\mu$m and a curvature radius of 190 ± 6 $\mu$m. The micro-lens array itself is 0.60 ± 0.05 mm thick, yielding a spot size of 6.2 ± 0.7 $\mu$m on the photosensitive component of the inductor.

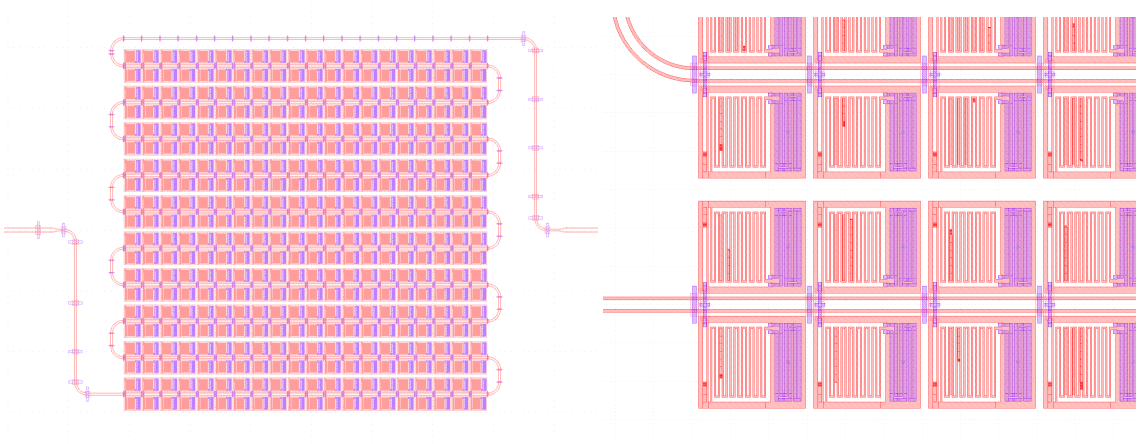

(a) $20 \times 20$ KID array (b) Multiplexed KIDs

Figure 3.2: Figure (**a**) shows the design of the $20 \times 20$ KID array in the chip designing software KLayout. A closeup of the bottom left corner in figure (**b**) shows the compact design of multiplexed KIDs. They are connected to the CPW readout line which runs across the entire detector in a zig-zag pattern. In this closeup, the variety in finger cut lengths is also visible. Since the IDC is shaded white, the incremental cutting is demonstrated by red shaded squared covering up a portion of the finger.

## 3.2 Multiplexing and F-scatter

Producing a system of multiplexed KID responses proves to be challenging because it is important to keep the frequency spacing $\phi = f_{0,n} - f_{0,n-1}$ between successive detectors both consistent and large enough to prevent the individual KID responses from appearing too close to each other on the same readout signal. When this happens, the response signals of individual KIDs risk overlapping. A direct consequence is that the two overlapping signals become indistinguishable, rendering any information each respective KID may provide unintelligible. With regards to the KID array, if there are KID signals overlapping with each other, the result would be a reduced pixel yield.
Even though the design of a KID array displays each KID with perfectly spaced resonance frequencies, the fabrication process is usually never good enough to guarantee the $f_0$-values across the KID array are as designed. This leads to an inconsistent frequency spacing. Typically, deviation from the designed resonance frequency $f_0 + \delta f$ can be measured, which may be referred to as the frequency scatter or f-scatter. A convenient measure of f-scatter present in a detector array is the standard deviation $\sigma_{\delta f/f}$ of fractional frequency deviation $\delta f/f$, a dimensionless property given by

$$\frac{\delta f}{f} = \frac{f_{0,\text{measured}} - f_{0,\text{design}}}{f_{0,\text{measured}}} \tag{3.1}$$

After recording the response of the KID array, a value for the standard deviation $\sigma_{\delta f/f}$ can be obtained, meant to quantify the severity of the f-scatter across the array. Such a measurement has been performed by Bhoedjang in their evaluation of f-scatter in $6 \times 6$ optical KID arrays, resulting in the lowest measured standard deviation of $\sigma_{\delta f/f} = 2.28 \cdot 10^{-3}$. However, the claim was made that the true value might be higher due to the occurrence of KIDs having swapped $f_0$. This was also evident in the observation that the maximum frequency spacing exceeded the designed average frequency spacing. It managed to emphasize that the f-scatter in a KID array therefore does not only act as a nuisance that needs reduction, but it risks the measured readout signal becoming indecipherable. [10]

## 3.3 Noise

In order to make strides towards examining the multiplexed signal for f-scatter, one must be aware of the noise sources that present themselves in a detector. The quality of the readout signal and that of the results are undeniably connected to one another. In this section, the focus is directed towards some of the most common noise sources in KIDs: generation recombination (GR) noise, amplifier noise, hot phonon loss noise and two-level system (TLS) noise. Of these four sources, the first two will be gone over for their relevance to this paper, as in later chapters they will prove to be one of the directing factors of measurement performance.

### 3.3.1 Generation Recombination Noise

Generation recombination (GR) noise is an intrinsic noise source of the detector and is caused by thermally driven fluctuations in the number of quasiparticles of a device in thermal equilibrium. It arises from the random process of quasiparticle generation and recombination into Cooper pairs, as mentioned in section 2.1. This grants it the classification as a fundamental noise source.
GR noise is typically considered a noise floor for KIDs since it is smaller than most other noises present in the KIDs detection response. With the increase of temperatures, the GR noise becomes more relevant. [11]

### 3.3.2 Amplifier Noise

Next to noise sources within the KID design, the amplifier noise, introduced by the electronic equipment for readout, is not less significant than the previous. In fact, because its origin lies in the random motion of electrons, it is incorporated in the amplified transmitted signal $S_{21}$ and does not arise from quasiparticle fluctuations, making it an external noise source. Therefore, this noise has a flat, white spectrum and can thus be modeled as an equivalent thermal noise source, characterized with an equivalent noise temperature $T_N$.
In Verheul's paper on the sensitivity of KIDs, the amplifier noise is shown to be directly related to the noise temperature $T_N$. Additionally, the dependency on the microwave readout power, $\propto P_{\text{read}}^{-1}$, was highlighted. An increased $P_{\text{read}}$ reduces the amplifier noise. However, it has been experimentally shown by De Visser et al. that the quasiparticle density $n_{\text{qp}}$, and therefore the quasiparticle recombination time $\tau_{\text{qp}}$, are dependent on $P_{\text{read}}$. As figure (3.3(b)) suggests, increasing the readout power causes an apparent increase in quasiparticle density and a subsequent decrease in lifetime. The increase of $P_{\text{read}}$ therefore results in an increase of GR noise. On the other hand, decreasing $P_{\text{read}}$ would increase the GR noise to the point where it is the dominating noise source and the greatest limiting factor in detection sensitivity. Hence, typically, a $P_{\text{read}}$ optimum needs to be observed in order to yield the best sensitivity of the device.

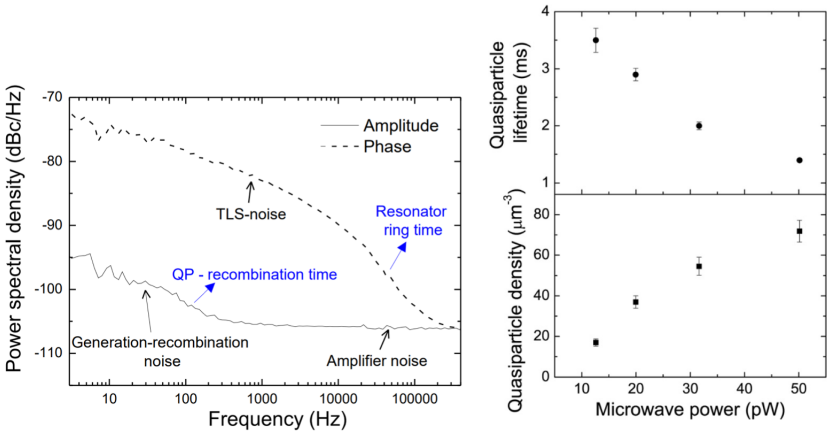


(a) PSD of noise in a KID

(b) Relation between $P_{\text{read}}$ and $n_{\text{qp}}$, $\tau_{\text{qp}}$

Figure 3.3: Figure (**a**) shows the power spectral density of measured amplitude and phase plotted against the frequency. Here the spectral power densities of the TLS, GP and amplifier noise are incorporated, which shows clearly the amplifier noise is a white noise. Figure (**b**) displays the weighted averages of 100-150 mK measurements of the quasiparticle density $n_{\text{qp}}$ and the recombination time $\tau_{\text{qp}}$ as a function of readout power $P_{\text{read}}$. Increasing the microwave power increases $n_{\text{qp}}$ and, in turn, a decrease in $\tau_{\text{qp}}$. [12]

# Chapter 4

# Optical System

This chapter will be entirely dedicated to the optical setup used in this paper. Bringing the optical setup to realization involved determining several criteria and limitations, which will be listed in the first section. The design of the optical setup will be broadly discussed with the assistance of theoretical optics. The main sources consulted for the relevant knowledge of optical systems, are the refined works on theoretical optics by Hecht [13] and Adam et al. [14].

## 4.1 Criteria and limitations

The main purpose of the setup is performing a scan of the KID array in the x- and y-direction to produce a spatial map of the array. The setup must be able to image a scan line projected on a display onto the KID array chip inside a cryostat, a near-absolute-zero cooling device discussed in the next chapter. Designing such an imaging system can be achieved by consulting geometrical optics and the branch of aberration optics. However, before commencing this design process, it is important to highlight all the criteria and limitations the design is subjected to.

1. **Minimum image distance of the scan line.** The KID array chip is located inside of a cryostat, where the distance between the chip and the entrance window amounts to 353.5 mm. This sets a lower limit to the image distance, as no optical element can be placed within this distance.

2. **Maximum step size of the scan line.** In this paper, the scan line is projected onto a display with a pixel size of 60 $\mu$m. The step size must allow the scan line to illuminate each and every row and column of KIDs. When the step size exceeds the dimensions of a single KID, 150 $\mu$m, the scan is likely to leave out some rows and columns. This puts an upper limit to the step size of the scan line, which is in accordance with the magnification of the image on the chip.

3. **Maximum spot size.** The image of the scan line onto the chip must have acceptable resolution. This implies that a single scan line targeted at a specific row of KIDs, must minimize the illumination of neighboring KIDs. A maximum spot size directs how sharp the image of the scan line needs to be on the chip for the appropriate illumination.

4. **Minimum scanning area.** The scan line on the display needs to be able to move across the entire chip, leaving out no KIDs in the process as mentioned earlier. As the dimensions of the KID array chip is $3 \times 3$ mm, the minimum scanning area can be marked with the same dimensions.

5. **Maximum height of the optical system.** The cryostat is suspended at a certain height with the entrance window located in the bottom, see figure (5.1). In this paper, the optical setup will be constructed on an optical table. The surface of this workspace reaches a height of 145 mm below the entrance window

at the bottom of the suspended cryostat. In order to allow the scan line to enter the cryostat, the optical setup must be constructed at a height below the maximum value of 145 mm.

6. **Maximum workspace.** As mentioned in the previous point, the setup is constructed on an optical table. The optical table that was available in the time period of this paper, was occupied to the point where only a maximum area of $700 \times 500$ m could be utilized for the construction of this setup. The design of this design therefore must take this limitation into account.
7. **Alignment measures.** When imaging the scan line onto the chip, one must be able to inspect if the scan line is properly aligned. A way to realize this, is by implementing a CCD camera in the setup. Moreover, the setup must have as many degrees of freedom with regards to setup adjustments. This implies the facilitation of changing the location of the display, CCD camera, imaging lens, etc.
8. **Resolution of the CCD camera.** When the chip is too small for the CCD camera to produce an sharp image of it, the alignment cannot be executed. This puts forth the criterion of a minimum CCD camera resolution.
9. **Availability of optomechanical components.** The design has to be built using off-the-shelf optomechanical components, provided by Thorlabs®. Therefore, the design must take into account the available optical system elements of the provider.

## 4.2 Lens System

This section presents several topics in geometrical optics that are involved in the creation of a lens system design. Based on this knowledge and the listed criteria, a design trade-off will be laid out in section 4.2.2.

### 4.2.1 Geometrical Optics

A light source is essentially a large collection of point sources, each of which produce a spherical wave that travels radially outward. Such spherical waves can be manipulated to converge and diverge though some arrangement of reflecting and refracting surfaces, lenses. If an image is desired from a point source, the spherical waves will need to converge on the image plane. In order to predict the behavior of a bundle of light rays through a lens, it is convenient to assume the bundle is made up of paraxial rays, rays that make a small angle with the optical axis, i.e. the symmetry axis of the system. Due to the introduction of this concept, Snell's law,

$$n_i \sin(\theta_i) = n_t \sin(\theta_t) \tag{4.1}$$

can be simplified by formulating the approximation $\sin(\theta) \approx \theta$. This allows the refraction through a single spherical surface with radius $R$ and refractive index $n$ to be expressed as

$$-\frac{n_1}{s_o} + \frac{n_2}{s_i} = \frac{n_2 - n_1}{R} \tag{4.2}$$

This forms the basis of the construction of the Lensmaker's formula, where the thin lens approximation is given by

$$\frac{1}{f} = (n-1)\left(\frac{1}{R_1} - \frac{1}{R_2}\right) \tag{4.3}$$

$$\frac{1}{f} = -\frac{1}{s_o} + \frac{1}{s_i} \tag{4.4}$$

The geometry of the Lensmaker's formula as described in equation (4.4), is based on a linear scale from $-\infty$ to $+\infty$ with the center of a thin lens with focal length $f$ at the origin. The object distance $s_o$ and image

distance $s_i$ from the lens are therefore not expressed as the absolute value, but rather as the coordinate with respect to the lens.
The value of $f$ can be positive, signifying a converging or convex lens, or negative, signifying a diverging or concave lens. Depending on $f$, not just the image and object location, but also the magnification of the lens system will behave accordingly, which can be expressed as

$$M = 1 - \frac{s_i}{f} = \frac{s_i}{s_o} \tag{4.5}$$

The position of an object with respect to the lens will also determine whether the image will be real or virtual, see figures (4.1(a)) and (4.1(b)).

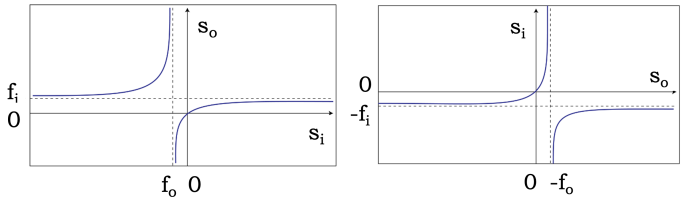


(a) Positive lens (b) Negative lens

Figure 4.1: The relation between $s_o$ and $s_i$ for (**a**) a positive lens and (**b**) a negative lens. The terms $f_o$ and $f_i$ are the object and image focal lengths of the lens respectively. [14]

Upon using two lenses with focal lengths $f_1$ and $f_2$, the optical path can be predicted similarly to a single lens system. By using equation (4.4) for each lens in the system, taking into account the location of the intermediate image becomes $s_{1i} - d$ with $d$ the distance between the two lenses, expressions for the image and object focal length can be constructed,

$$f_i = \frac{(f_{1i} - d)\, f_{2i}}{f_{1i} + f_{2i} - d} \tag{4.6}$$

$$f_o = -\frac{(f_{2i} - d)\, f_{1i}}{f_{1i} + f_{2i} - d} \tag{4.7}$$

respectively.
In the limit where $f_{1i} + f_{2i} = d$, the focal lengths approach infinity and the optical rays run parallel to each other in the light bundle, also called a collimated beam. Such a system is called a telecentric lens system.
In the limit where $d \to 0$, the focal length will satisfy the relation $1/f = 1/f_{1i} + 1/f_{2i}$. By construction using the intermediate image, the magnification of a two lens system is the product of the magnification of the two lenses: $M = M_1 M_2$.

### 4.2.2 Design Trade-Off

Using the provided geometrical optics, three separate lens systems are designed and discussed. Eventually, the system that best complies with the criteria and limitations, listed in section 4.1, will be decided for implementation.

#### 4.2.2.1 Telecentric Lens System

As point 1 in section 4.1 states, there is a minimum imaging distance of $s_i = 353.5$ mm, which is the distance between the KID array chip and the entrance of the cryostat. One has to take into account the distance required to guide the light bundle from the horizontal setup into the vertically suspended cryostat, which is done using a right angle mirror. For simplicity, the fixed image distance is taken as $s_i = 600$ mm, which will form the starting point for each of the calculations performed in this setup.

Ideally, the magnification of the lens system is $|M| < 1$, indicating that the image of the scan line on chip is smaller than its projection on the display. This allows for more freedom in scan line settings such as the maximum step size, described in point 2 in section 4.1. One way to achieve this is by using the aforementioned telecentric lens system, see figure (4.2). The convenience of this lens system is that the magnification is described in terms of the focal lengths of each lens, $M = f_{2i}/f_{1i}$. This makes the decision of what focal lengths to use for a desired magnification, quite easy. However, the minimum image distance forces the object distance to be $s_o = s_i + d$. When a smaller magnification is desired, $d$ will increase and, ultimately, cause $s_o$ to increase, $s_o \propto |M|^{-1}$. In order to prevent the optical setup from exceeding the limited area on the optical table, mentioned in point 6 in the previous section, this proposal was rejected.

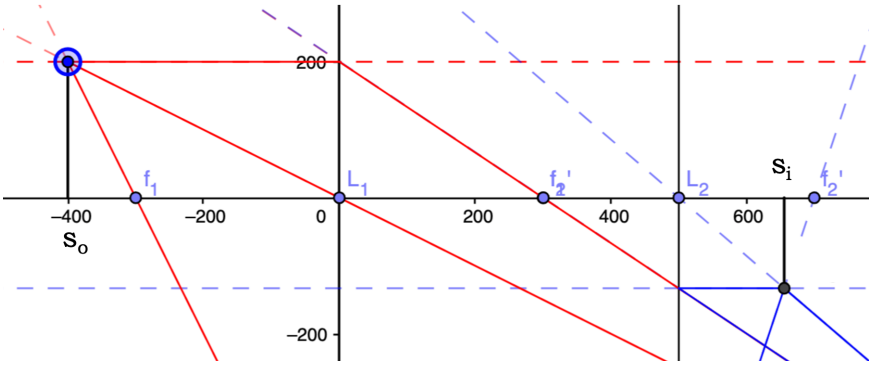


Figure 4.2: A simulation of a telecentric lens system with $|M| = f_2/f_1 = 0.5$. The characteristic of a telecentric lens system is the distance between two two lenses $d = f_1 + f_2$.

#### 4.2.2.2 Virtual Imaging Lens System

The next lens system exploited virtual imaging using one positive lens and one negative lens, see figure (4.3). This design is more promising as it allows for a reduced $|M|$ whilst keeping $s_o$ as small as possible. In spite of this, it was decided to discontinue the consideration of this design. The first reason for this is concerns practicality, as it would impose an overly meticulous alignment procedure. The second and more important reason for dropping this design, is because the lens system would need multiple stages of development to meet the set requirement upon construction. This was considered unrealistic from a time management point of view.

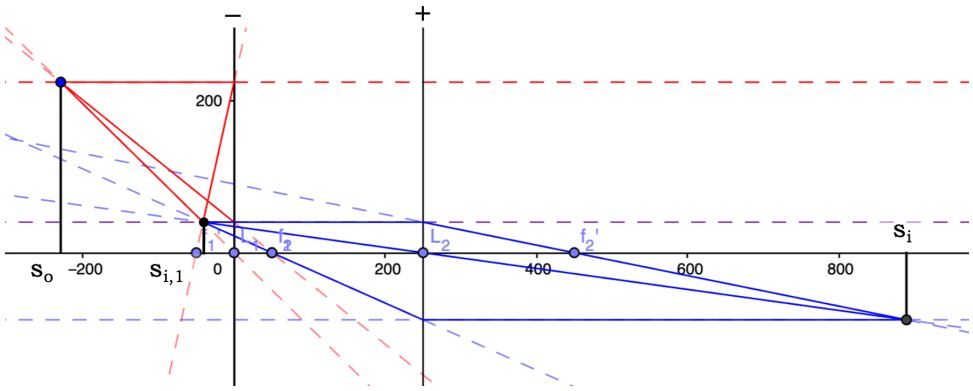


Figure 4.3: A simulation of a lens system considered for implementation into the optical setup. This system produces a small intermediate virtual image $s_{i,1}$, which can then be enlarged to produce a real image onto the KID array chip $s_i$. This simulation was constructed to present the ability to produce an image with $|M| < 1$ at $s_i > s_o$.

#### 4.2.2.3 Single-Lens System

The third and last system that is explored for the design of the optical system is a single-lens system. The focal length $f$ for the only present lens was based on the pixel size of the display. The pixels of the display are 60 $\mu$m in size, which is only a factor 2.5 smaller than a single KID. The single-lens system is desired to keep the image magnification $|M|$ as small as possible so the pixel image size does not exceed the size of a single KID, 150 $\mu$m. This allows for a more flexible scanning procedure, as the line width and step size of the scanning line can be adjusted more freely. However, equation (4.5) shows that for $|M| < 1$ the object distance would rapidly exceed 600 mm, which forces the setup to require a larger workspace area than available. Therefore, a one-to-one imaging system is chosen where the only present lens has a focal length of $f = 300$ mm. The magnification of the image becomes $M = -1$, which allows for a maximum step size of the scan line to become 2.5 px.

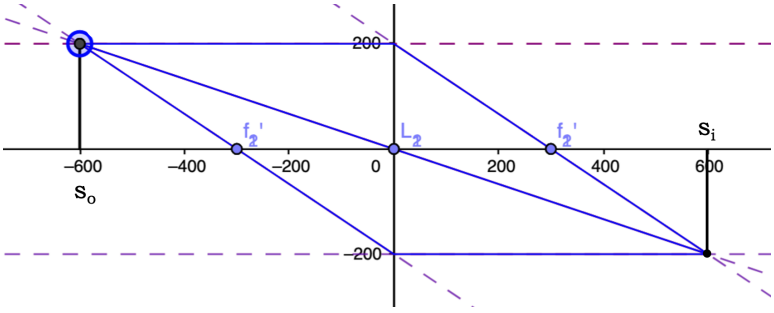


Figure 4.4: A simulation of the single-lens design, chosen to be implemented into the optical setup. The one-to-one imaging is realized by implementing a lens with focal length $f = 300$ mm and $s_o = s_i = 600$ mm, providing a magnification of $M = -1$.

## 4.3 Correcting Aberrations of the Lens System

A single-lens system introduces imperfections into the imaging process, which are known as optical aberrations. By simulating the single-lens system in the optical design software Zemax®, one can determine the aberrations affecting the image. To acquire a better understanding of how optical aberrations work,

the theoretical optics of aberrations will be gone over. This is followed up by a summary of the properties of aperture stops (section 4.3.2.1), and how an aperture stops is utilized in the optical setup to reduce the effects of aberrations (section 4.3.2.2).

### 4.3.1 Optical Aberrations

When designing advanced optical systems, one will notice a significant inconsistency of the behavior of optical rays according to Gaussian geometric optics. Non-paraxial rays will also play a role in the final image production. This departure from the idealized conditions of Gaussian optics are known as aberrations, of which there are two types: chromatic aberration, describing image deteriorating effects of "multi-colored" light, and monochromatic aberration, which only concerns light of only a single-wavelength or with a narrow spectral bandwidth.
The monochromatic aberrations exhibit five kinds of aberrations, known as the primary or Seidel aberrations: spherical aberration, coma, astigmatism, field curvature, and distortion. As previously mentioned, a detailed overview of each of the optical properties and practical aspects of aberrations can be found in the theoretical optics handbook by Hecht. However, this paper concerns only chromatic aberration and the last two Seidel aberrations, which will be discussed shortly.

#### 4.3.1.1 Field Curvature

Due to the insufficiency of the paraxial ray approximation, imaging a planar object results in an image affected by field curvature or Petzval field curvature, see figure (4.5(a)) for a visualization. The axial object focal points and the focal points of off-axis light rays are not aligned on a planar image surface, but rather on an paraboloid image surface. The farther off-axis the light rays, $y_i$, the larger the deviation from the planar image surface, $\Delta x$. This misalignment produces an image with a defined center and blurred edges. This implies that somewhere on the optical axis, in between the axial ray focal length and the peripheral ray focal length, a spot size can be found of optimal resolution, known as the circle of least confusion (4.5(b)). This concept is applicable to all Seidel aberrations and is defined as an image plane where the imaging resolution is at its peak despite the aberration effects.

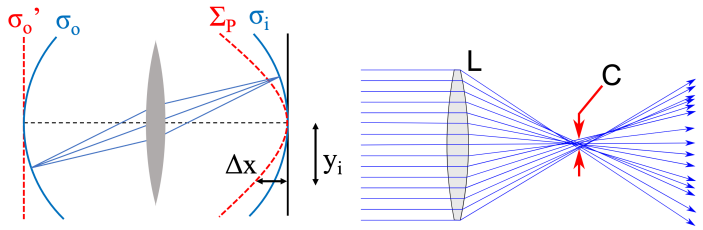


(a) Field curvature (b) Circle of least confusion

Figure 4.5: Figure (**a**) displays the paraboloid image surface, or Petzval surface $\Sigma_P$, of a planar object $\sigma_o'$. The deviation of a light ray from the optical axis $y_i$ manifests in a deviation in focal length $\Delta x$ from the planar image surface. [13] Figure **b**) provides a visualization of the circle of least confusion in spherical aberration, but is applicable to every Seidel aberration. The circle of least confusion is labeled as C. [15]

#### 4.3.1.2 Distortion

Distortion originates from an off-axis image distance leading to a transverse magnification, $M_T$. Therefore, distortion arises when different areas of the lens have different focal lengths and subsequently different magnifications. When an image suffers from positive of pincushion distortion, each image point is displaced radially outward from the center as displayed in figure (4.6(a)). Contrasting is negative of barrel distortion, where the image points are radially pulled inward towards the center. This effect also accompanies the

introduction of an aperture stop into a thin lens system, which be explored in the next section specifically dedicated to aperture stops.

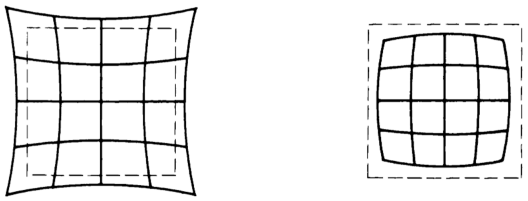

(a) Pincushion distortion (b) Barrel distortion

Figure 4.6: Figure (**a**) shows the pincushion effect on the image produced using a positive lens. The edges of the mage are extended radially outward compared to the dashed rectangle, representing the non-distorted image. Figure (**b**) shows the barrel distortion, which occurs when using a negative lens.

#### 4.3.1.3 Chromatic Aberration

As previously mentioned, the five primary or Seidel aberrations only apply to monochromatic light, or to light with a relatively narrow spectral bandwidth. When looking at polychromatic light, equation 4.3 is a function of the refractive index of the lens material, which in turn is dependent on wavelength, $n(\lambda)$. A larger wavelength will achieve a smaller refraction angle $\theta(\lambda)$ resulting in blue colored light having a much shorter focal length than red colored light. Therefore, different colored light will pass through an optical system along different paths. The effects of chromatic aberrations are easy to observe. When a bundle of polychromatic light traverses a convex lens, it will cast an image surrounded by a halo.

### 4.3.2 Implementing Aperture Stops into the Setup

#### 4.3.2.1 Aperture Stops: Theory

The largest contributors of image degrading aberrations arise due to off-axis light rays. In order to minimize the aberration effects, one may refer to the use of an adjustable aperture stop in the system.
Aperture stops are optical elements which determine the collection of rays that will ultimately contribute to the image formation. It dictates what portion of the incoming or outgoing light cone is included, reflected in the entrance pupil of the optical system, and which portion is excluded, reflected in the exit pupil. [14] These components can be described entirely using geometrical optics from section 4.2.1. Optical elements that may function as the aperture stop are the rim of a lens or a diaphragm iris.
The aberration resolving properties of an adjustable diaphragm iris as an aperture stop are dependent on its placement and diameter. By consulting the chief ray, a light ray which fundamentally passes through the center of the aperture stop, the location of the aperture stop on the optical axis can be determined. Determining the diameter of the aperture stop can be done by looking at the marginal ray, which passes along the rim of the aperture stop.

#### 4.3.2.2 Aperture Stops: Correcting Aberrations

Field curvature typically goes hand in hand with astigmatism, which also arises due to off-axis light rays. In order to minimize their combined effects, two lens systems involving an aperture stop can be considered: an orthoscopic lens system and a telecentric lens system, see figures (4.7(a)) and (4.7(d)) respectively. The latter is capable of effectively eliminating the field curvature and the accompanying astigmatism. However, one needs to be reminded of section 4.2.2, where the design of a telecentric lens system was dropped due to the excessive workspace area it required. For this reason, the orthoscopic lens system is considered for implementation.

In the orthoscopic lens system, the aperture stop is placed directly against the single lens. Here the chief ray runs right through the center of the lens. The peripheral light rays suffering the largest deviation in refraction from the light rays of the paraxial region, will then be excluded from the light cone used to produce an image. This will in turn increase the resolution of the circle of least confusion, see figure 4.5(b), and in turn reduce the image spot size, expressed in point 3 in section 4.1.

As mentioned in section 4.3.1.2, the location of the aperture stop with respect to the lens is accompanied by distortion. Placing the aperture stop at considerable distance before the single lens will result in barrel distortion, see figure (4.7(b)). On the other hand, placing it behind the lens results in pincushion distortion, see figure (4.7(c)). In order for a stop to be implemented into the single-lens system without worsening the distortion, the stop should be placed directly against the lens. This is precisely in line with the orthoscopic lens system in figure (4.7(a)), which was suggested for field curvature correction.

While a smaller diameter of the aperture stop may block out most aberration imposing light rays, the scanning area must remain sufficient for the entire KID array chip to be scanned. Returning the the provided criteria and limitations listed in section 4.1, the size of the aperture must not shrink to below the dimensions of the chip, $3 \times 3$ mm. A diameter of $D = 2 \times \sqrt{1.5^2 + 1.5^2} = 4$ mm$^2$ would therefore set the lower limit of the scanning area. However, since an aperture with this diameter would deprive the image of sufficient brightness, meeting this lower limit is unlikely.

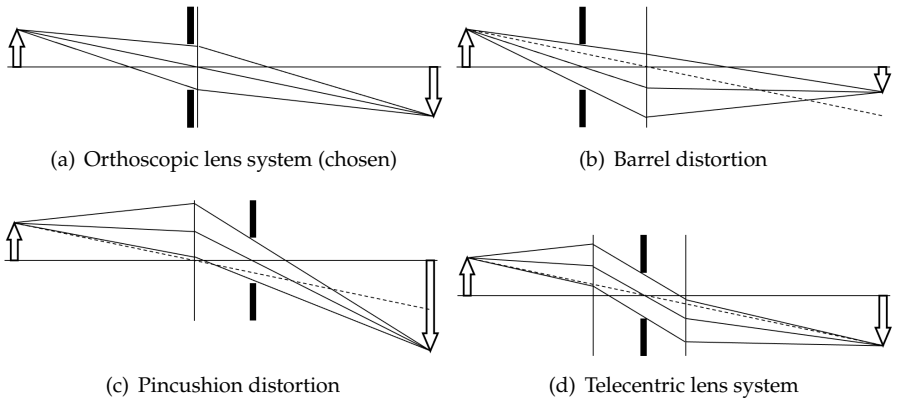

(a) Orthoscopic lens system (chosen)

(b) Barrel distortion

(c) Pincushion distortion

(d) Telecentric lens system

Figure 4.7: There are several lens diagrams presented where the placement of the stop is varied, resulting in pincushion distortion (**b.2**) and barrel distortion (**b.3**). The lens diagrams in figures (**b.1**) and (**b.4**), orthoscopic and telecentric systems respectively, have a reduced distortion in the final image. Of the two corrective systems, the orthoscopic lens system was chosen due to the fact that it requires a single-lens system.

### 4.3.3 Zemax Simulation

By simulating single-lens system in the optical design software Zemax®, the accuracy of the system can be investigated. Additionally, the reduces spot size can be examined for influence of any aberrations. This is done for both the uncorrected and the corrected optical system, figures (4.8(a)) and (4.8(b)) respectively. By comparing the spot sizes between the two collections of point spread diagrams, the resolution of the image can be recognized to be improved.

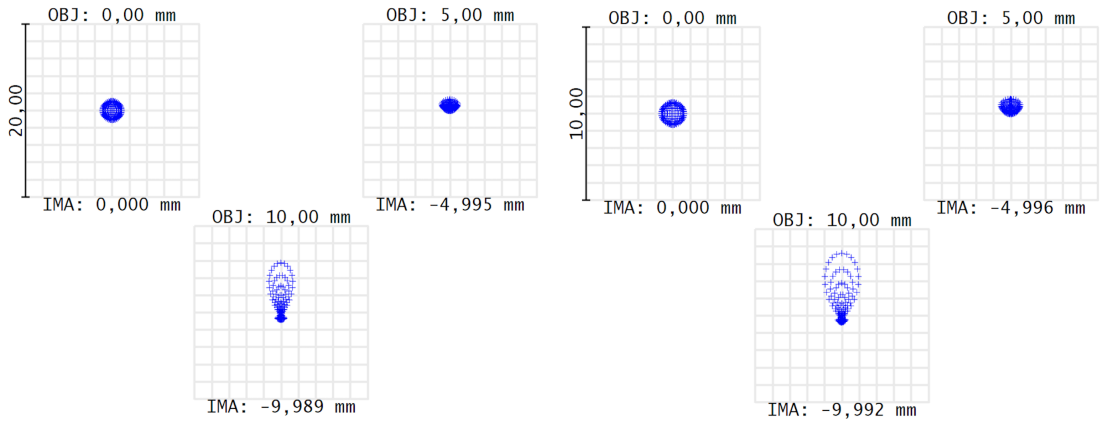


(a) Point spread diagrams before correction

(b) Point spread diagrams after correction

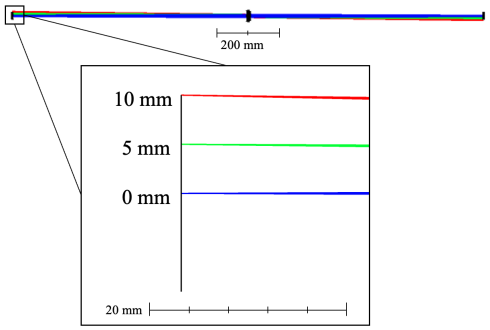


(c) Lens simulation closeup

Figure 4.8: Figure (**a**) shows point spread diagrams obtained from simulating the single-lens system before implementing an aperture stop. These diagrams show the spot size for three object heights: 0 mm (optical axis), 5 mm and 10 mm. Figure (**b**) shows the same point spread diagrams, only for the orthoscopic single-lens system. Comparing the two shows there is a decrease in spot size due to the introduction of a stop with a 10 mm diameter. Figure (**c**) shows a closeup of the point objects, where the mentioned object heights are represented respectively by blue, green and red rays.

## 4.4 Alignment: mechanical design

As previously mentioned, the setup is designed using optomechanical components from Thorlabs®, all of which are displayed in Appendix B. This section focuses on creating as many degrees of freedom as possible, by implementing various mechanical adjustment opportunities into the designed setup, displayed in figure (4.9).

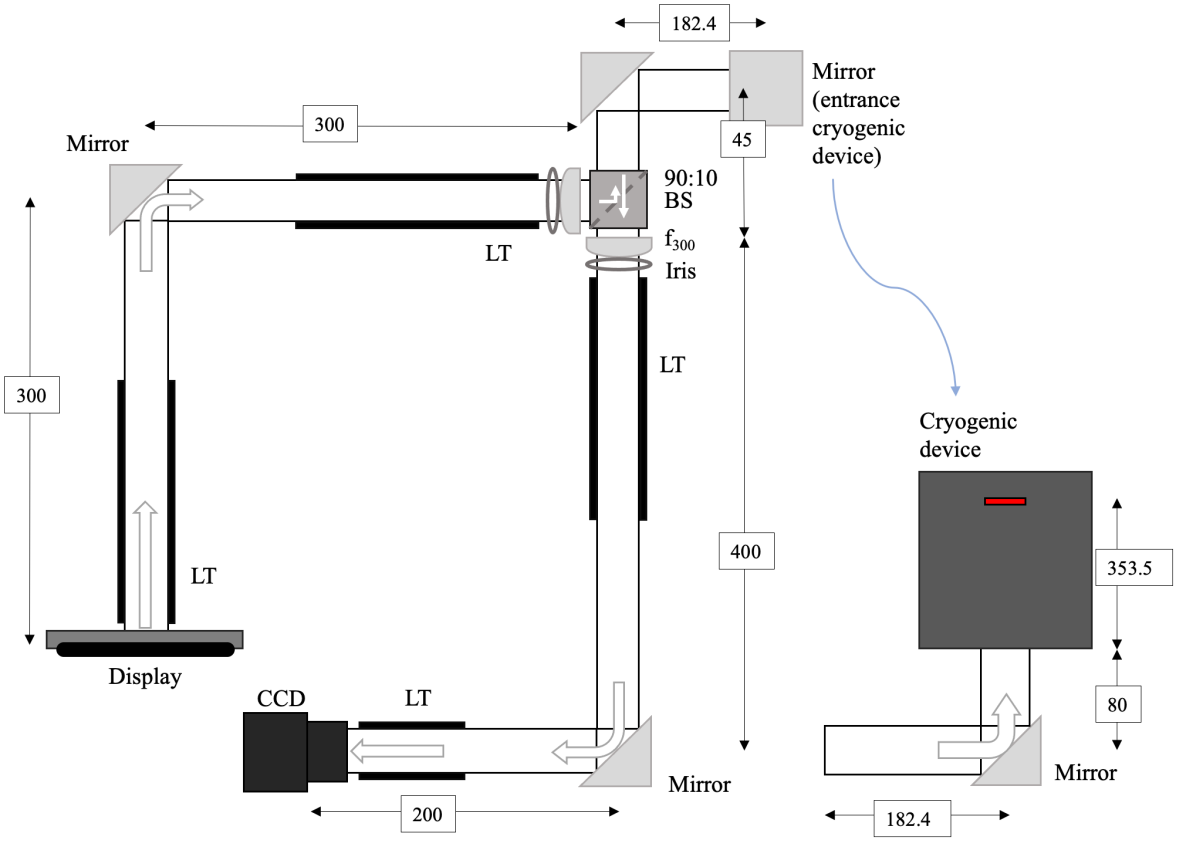


Figure 4.9: Schematic overview of the final setup. The setup construction on the left shows a top view of the optical system, used to image a scan line on the KID array chip. The setup construction on the right displays a side view of optical setup, specifically the portion responsible for directing the light into the cryostat. Here this the KID array chip is shaded red. The lens tubes, labeled with LT, block stray light from interfering with the imaging process. The distances noted along the light path are expressed in mm.

### 4.4.1 CCD Camera

Firstly, a CCD camera is implemented to facilitate alignment of the scan line onto the KID array chip, mentioned in point 7 and 8 of section 4.1. In this paper, the Backfly S USB3 was used as a CCD camera. This device has a resolution of $720 \times 540$ px with pixel size 6.9 $\mu$m, which provided sufficient resolution for imaging the $3 \times 3$ KID array chip with $|M| = 1$.
A two-armed optical system is designed to accommodate this CCD camera. The two arms, one reserved solely for the display and the other for the CCD camera, will be functioning as two independent single-lens optical systems, where the length of each of these arms has to be approximately $s_o = s_{i,2} = 600$ mm to produce a sharp one-to-one image. To make sure each arm can be operated independently from the other, each arm will have one lens installed.
The beamsplitter connecting the two arms is a 90:10 beamsplitter, located in the top right of the final design top view. This beamsplitter transmits 10% of incoming light into the cryostat to ensure the individual KIDs receive enough illumination power during the scanning measurements, and refracts 90% of returning light towards the CCD camera for sufficient image capturing.
Furthermore, the need for more space than the available workspace can be eliminated by installing right-angle mirrors around half-way along each arm.

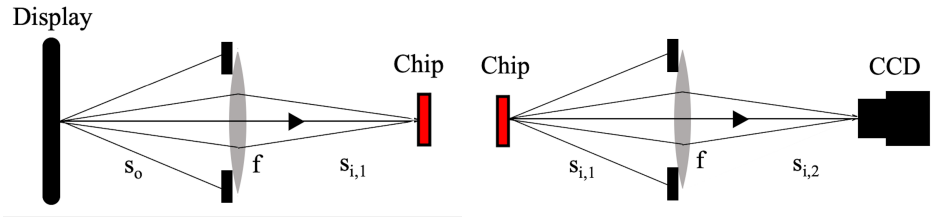


(a) Display arm (b) CCD arm

Figure 4.10: Schematic images of the one-to-one optical systems of the display and the CCD camera.

### 4.4.2 Adjusting Arm Lengths

Secondly, an extendable cage system mechanism for both the display arm and CCD camera arm is designed, displayed in figures (4.11(a)) and (4.11(b)) present. This is to facilitate longitudinal movement of both the CCD camera to obtain a sharp image of the KID array chip inside the cryostat, and the display when the theoretical and practical the $s_o$ and $s_{i,2}$ do not match exactly.

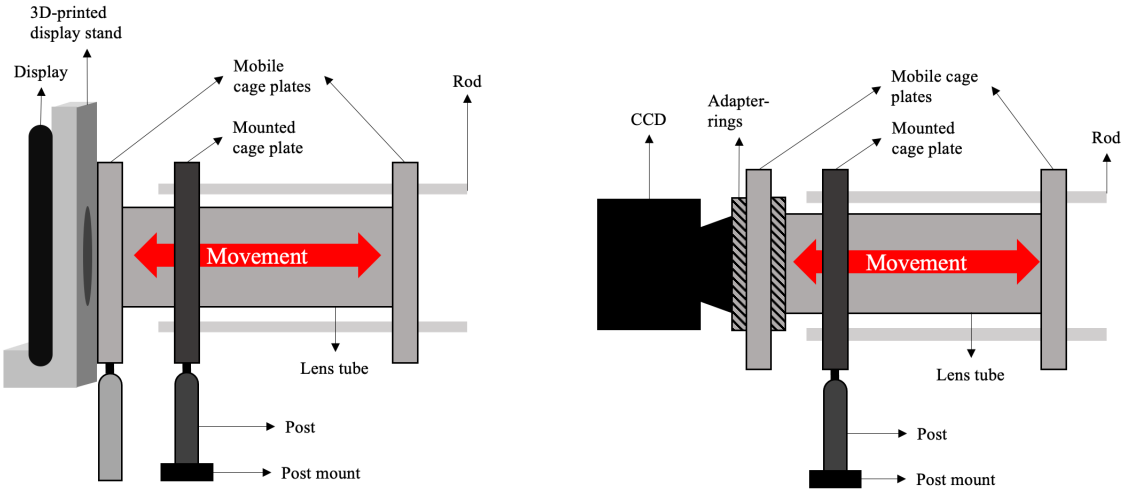


(a) Display extension (b) CCD extension

Figure 4.11: Designs for the extendable cage systems for both the display and the CCD camera. The dark shaded components are mounted to the rods and the optical table as a means of keeping the cage system in place. The light shaded components are not mounted to the rods, nor to the optical table, nor to the mounted components. This allows them to slide through the mounted components when attempting to achieve a sharp image. The lens tubes in both systems are screwed onto a cage plate with rods driven through it. This minimizes transversal movement when adjusting the extension. The 3D-printed display stand in figure (**a**) has a cage plate directly mounted onto it, which facilitates a rigid connection to the lens tube. In figure (**b**), two male-to-male adapter rings have been screwed onto either sides of a cage plate to connect the CCD camera to the lens tube.

### 4.4.3 Degrees of Freedom

Lastly, a degree of freedom at the cryostat entrance is introduced in the form of a kinematic mirror. The advantage of using a kinematic mirror is that it can move light beam with much more precision and ease than simply moving the optical table.

The kinematic mirror allows for rotational movement in the display imaging on the KID array chip, and CCD imaging of the chip. Given the distance between the single-lenses and the chip is relatively large compared to the image size, only small rotations are necessary to align the optical system with the chip. These small rotational movements could therefore be approximated as translational movements.

The three alignment methods presented in this section provide a six degrees of freedom, all of which are listed below.

- x-translation: placement of the imaged scan line on the KID array chip. This is facilitated by moving the optical table in the x-direction.
- y-translation: facilitated in a similar fashion as x-translation.
- z-translation: adjusting $s_o$ $s_{i,2}$. This is facilitated by the extendable cage systems in figures (4.11(b)) and (4.11(a)). These are considered z-translations because they can be moved closer or farther from the KID array chip.
- x-rotation: preciser placement of the imaged scan line on the KID array chip. This is facilitated by the kinematic mirror. Due to the small angle of rotation, this may be approximated as x-translation.
- y-rotation: facilitated in a similar fashion as x-rotation.
- z-rotation: orientation of the setup. This is facilitated by rotating the optical table.

With regards to the remaining details of the mechanical design, all optomechanical components from Thorlabs® used to design the setup construction, have been dedicated entirely to a 30 mm cage system. In order to comply with point 5 of section 4.1, the cage system was installed on the optical table using 50 mm tall posts. This allowed the optical system to comfortably fit below the entrance window of the cryostat with a separation of 65 mm.
Using the dimensions of the optomechanical components, the light path from the singe-lenses to chip can be summed up to $s_{i,1}$ = 660.9 mm, which is taken as a fixed length. In order to produce a one-to-one image, the light path from the single-lenses to the display and CCD camera, $s_o$ and $s_{i,2}$ respectively, must approximate this distance. Thanks to the cage system extensions in figure (4.11), achieving this is relatively easy.

# Chapter 5

# Experiment

The previous chapter gave a thorough description of the optical system, which makes up a large part of the setup. Numerous times, a cryogenic device and a display were mentioned without providing proper background information. In fact, the information necessary to guide the design of the optical system was filtered out for the sake of transparency. This chapter, however, provides a more complete summary of the display, cryogenic device and the accompanying readout system, as they are crucial setup components. After these aspects of the setup are cleared up, the designated measurement procedure will be gone over, followed by the layout for the appropriate data analysis to interpret the obtained measurements.

## 5.1 Cooling method

As mentioned in section 2.1, the chip with the KID array on it has to be cooled down to its critical temperature, $T_c$ = 1K, for the detector to exhibit its superconductive properties. This is achieved by mounting the chip inside a dilution refrigerator, a cryogenic device that provides continuous cooling at near absolute zero temperatures. A cross section of the Bluefors® cryostat is shown in figure (5.1). As visible in this cross section, the cryostat is comprised of four vacuum pumped temperature stages labeled as the '300 K', '40 K', '4 K' and '100 mK' stage, moving inward. The stages are separated from each other by an aluminium shield. In the 100 mK stage, however, there is an additional light-tight container called the sample stage, which is where the detector is located within the cryostat.
The principle of dilution refrigeration rests upon circulation of gas mixture consisting of $He_3$ and $He_4$, of which a thorough description is available in the published article by Pradhan et al. The essence of this principle is that the stages are cooled down to 4 K, after which the $He_3$-$He_4$ dilution further cools the sample stage below 1 K. The continuous diluting and condensation on which the dilution refrigerator operates, makes the duration of the cooling process quite lengthy, as it can take up to a day to cool down the cryostat. [16]

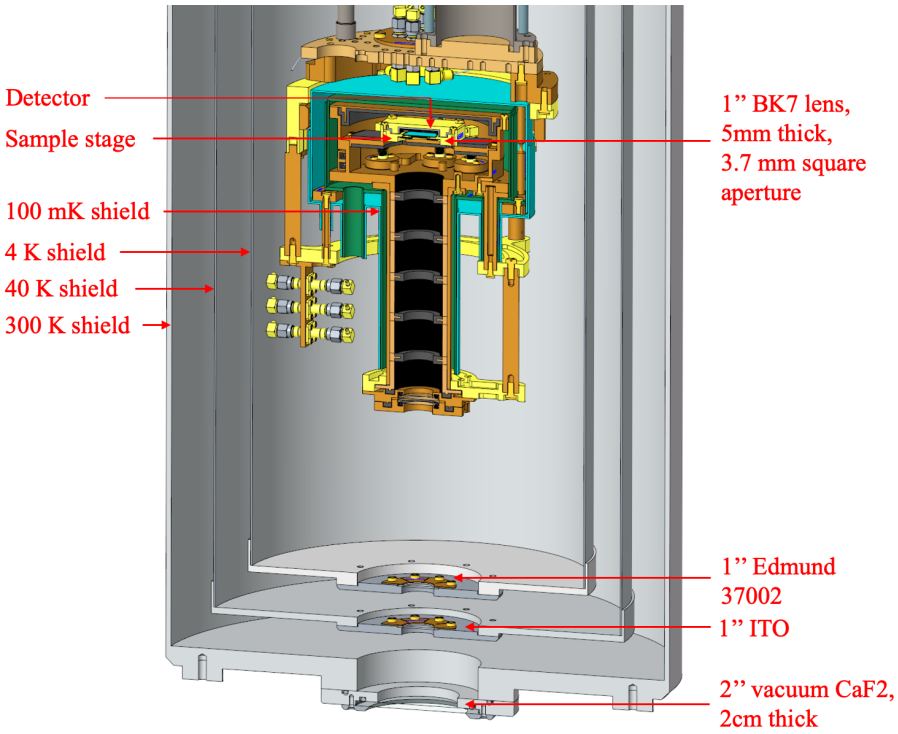


Figure 5.1: The cross section of the dilution refrigerator by Bluefors® used in this paper. The cryostat is used as an open setup in this paper, meaning it receives light from an external source. To realize this, each of the shields, except for the 100 mK shield, has a window which directs incident light into the sample stage. The 300K stage has a vacuum window, which is necessary for the cooling procedure to sustain itself. In total, the incident light has to travel 353.5 mm past the vacuum window in order to reach the detector. [1]

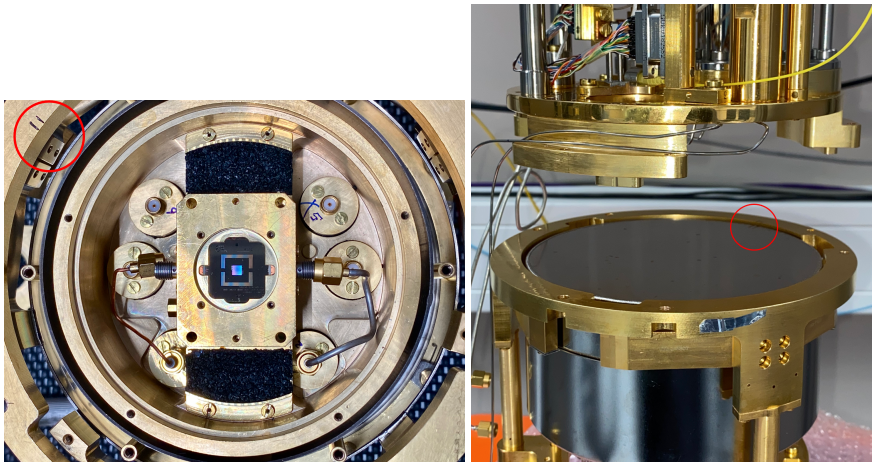

(a) Sample stage with mounted detector (b) 100 K stage

Figure 5.2: Pictures of the sample stage during the cryostat assembly. Figures (**a**) and (**b**) both have a red circle around the sample stage alignment demarcation, which allows the assembler to keep track of the orientation of the chip.

## 5.2 Readout System

Readout of the KID array inside the cryostat is done by homodyne detection, of which a description of the entire process is provided in great detail by Ras in their thesis on MKIDs for the MIR [1]. To perform a measurement, an electrical signal is generated and then split into two parts: one is sent to the IQ-mixer, the other is sent through the sample at the 100 mK stage. After the signal has passed through the resonators, the response is amplified multiple times both inside the several cryostat stages and outside the cryostat. Eventually, the amplified signal arrives at the IQ-mixer and is combined with the original signal. Notable is that the most dominant noise contribution at this point comes from the amplifier noise, discussed in section 3.3.
The resulting mixed signal is readout and interpreted by a vector network analyzer (VNA), which introduces several readout parameters with each their own effect on the readout signal quality: the readout power, the bandwidth per scan, the number of points per scan and the IF bandwidth.

### 5.2.1 Readout power

The first parameter, the readout power $P_{\text{read}}$, was mentioned previously in section 3.3.2 for its relation to quasiparticle density $n_{qp}$ and quasiparticle lifetime $\tau_{qp}$. The conclusion was that a higher $P_{\text{read}}$ is accompanied by an increase of GR noise, which puts an upper limit on the $P_{\text{read}}$. On the other hand, reducing $P_{\text{read}}$ allows the amplifier noise to dominate the readout signal, which sets a minimum for $P_{\text{read}}$. An optimum value needs to be achieved, which can be found through experimentation.

### 5.2.2 Bandwidth per Scan

The bandwidth represents the difference in frequency between the upper and lower limit of a frequency band. When the bandwidth is decreased, the measurement instrument allows for more data points to be collected across the fixed frequency band. A larger bandwidth increases the distance between measurements resulting in less data points per scan and therefore a less precise measurement.

### 5.2.3 Number of Points per Scan

The number of points per scan dictates how much detail of the detector response is desired to be captured. Adding more points per scan increases the chance of plotting the dips accurately. However, the amount of noise is also captured when increasing the number of points per scan. Nonetheless, the precision earns a higher priority than the disruption of noise, which may be filtered though other measurement settings or compromised during the data analysis.

### 5.2.4 IF Bandwidth

The last parameter, the integration frequency (IF) bandwidth, determines how many points are measured per second across a specific portion of the entire frequency band. This is inversely related to the integration time of the signal across that portion, $f_{\text{IF bw}} \propto t_{\text{int}}^{-1}$. A smaller IF bandwidth therefore yields a longer integration time, resulting in a smoother readout signal.

## 5.3 Display

The setup designed in this paper makes use of the Optic AMOLED display of the OnePlus 6T smartphone model. This display was chosen to perform the scanning measurements of the KID array for the following reasons:

- True black can be achieved. Because no backlight assembly is needed, the display can power off pixels that are to display the black portions of an image, meaning the black is as dark as it can be. This remarkably reduces the probability of the display illuminating untargeted KIDs, leading to a more contrasting KID response to light exposure.
- This OnePlus 6T model offers a maximum brightness of 431 cd/m$^2$. Testing throughout the construction of the setup have pointed out that a KID shows a detectable response deviation when illuminated by a scanning line projected on the display.
- The display slightly less than 157.7 mm tall and has a resolution of 2340x1080 px. Individual pixel size 60 $\mu$m, which is a factor 2.5 smaller than the size of an individual KID. For one-to-one imaging, this implies slight flexibility in both the scan line width and step size.

As the last item in the list above points out, the image of a single display pixel is not much smaller than a single KID. This implies that the smallest details of the AMOLED display will have a great effect on the detector array response. For this reason, the pixel design will be gone over in this section. This section also covers the software that was constructed for the remote operation of the display.

### 5.3.1 Pixel Layout Design

In order to explore the display in finer details, it is placed under a microscope, which exposes the pixel grid behavior for certain settings. The display was examined with several settings, of which images are displayed in figures (5.3(a-c)).

Visible in figure (5.3(a)), the pixels of the display form a diamond pattern in an arrangement known as the PenTile RGBG matrix, meaning blue and red pixels alternate each other with interleaved green pixels throughout the display. Therefore, projecting a green line with a 1 px line width produces a different pixel arrangement than the projection of a blue or red line with the same line width, see figure (5.3(b)). Also visible in this this figure is the subtle illumination of red pixels for an all-green line projection, of which the exact cause or purpose is not entirely clear. Yet, it may present some alterations to the power spectrum of the scanning line when imaged onto the KID array chip.
The pixel grid also shows that projecting a 1 px wide horizontal line requires two pixel rows in the colors red and blue, while it only requires one green pixel row. However, the green pixel pattern also shows a distinction between a vertically and a horizontally projected 1 px line. The horizontal line has two subtly red pixel rows, while the vertical has only one but slightly brighter red pixel row.
Due to this distinction, the power of a vertical scan line imaged onto the chip, is therefore slightly smaller than the power of a horizontal scanning line. This will undeniably be reflected in the magnitude of the individual deviating KID responses.

Next to colors, the behavior of various line widths is inspected. As demonstrated in figure (5.3(c)), the display increases the line width by stacking a row of pixels above and below the preexisting row in alternating fashion. This technique is applied on both the x- and y-direction diamond pattern.

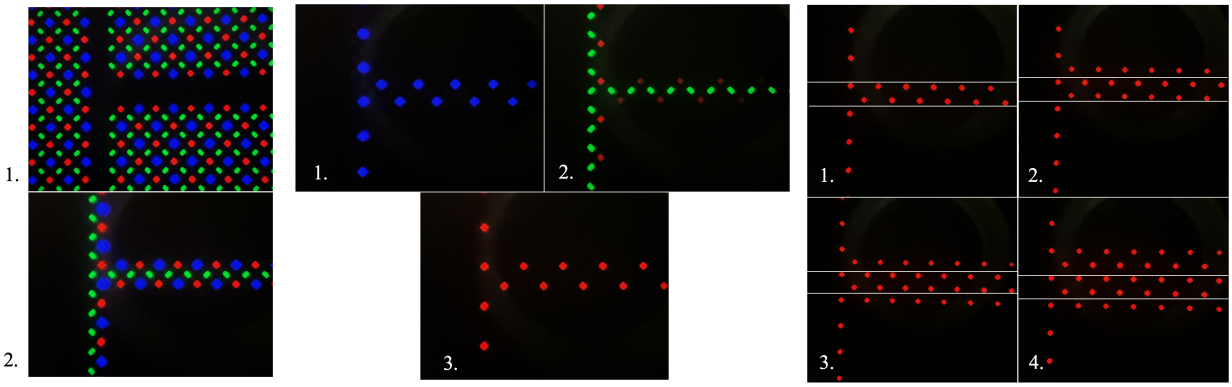


(a) Pixel arrangement: white (b) Comparing colors, RGB (c) Comparing line width

Figure 5.3: Figure (**a.1**) & (**a.2**) a microscopic view of the pixel arrangement on the Optic AMOLED display for a white light projection. In figures (**b.1-3**), the pixel arrangements the projection of a 1 px line in the colors red, green and blue are displayed for comparison. Figures (**c.1-4**) present the projection of a horizontal red line with widths 1, 2, 3 and 4 px, and a vertical line with width 1 px. On each of the four images, two horizontal lines are overlaid to mark the 1 px line width. This makes it easier to observe the technique that is used to increase the line width.

### 5.3.2 Remote Scanning Operation Software

The display functions as the light source illuminating the KID array chip in a scanning style. In order to realize this scanning behavior and adjust the scan settings on the display of the OnePlus 6T smartphone model, a remote operation software was designed, inspired by the paper by Bottom et al. [17]. This software was built into an app using the pygame and kivy module, designated for framework development of applications. These modules allowed for the settings of the scan line to be programmed in Python language. By connecting the smartphone to a computer via USB, the Python script and the display could communicate. The display could then be operated and adjusted to project a straight line which behaved like a scan line. The settings implemented in the scan line app are listed below.

- Step size dX and dY
- Line width
- Color cycle: `white` → `blue` → `green` → `red` → `off`
- Clearing the display by returning the X- and Y-scanning lines to their default position
- Assigning a number of scans
- Quit and Save operations

## 5.4 Measurement Procedure

This section is focused on how the measurements are done using the setup displayed in figure (4.9).
The first step towards obtaining successful measurements, is the alignment. Returning to the listed degrees of freedom in section 4.4, each of the listed measures need to be taken to make sure the optical setup is able to image a scan line onto the KID array chip with sufficient resolution.
Once the alignment is completed, it is important to darken the room in which the experiment is conducted, as much as possible. Stray light that interferes with the light coming from the display can have large effects

on the quality of the KID responses. In this paper, simply rolling down blackout blinds before all the windows and turning off the ceiling lighting was sufficient. Ideally, the control interfaces are displayed on remote monitors so any computer screens inside the room can be turned off for an even smaller chance of stray light interference.
The remote operation software of the display and the VNA, used in this paper, were programmed and synchronized to have the self-monitored capability to:

1. Schedule the number of scans per coordinate axis (x or y) that need to be performed across the KID array;
2. Position the scan line with a decided line width, color at a designated coordinate;
3. Capture the multiplexed KID array response for the designated coordinate of the scan line, and save the measurement data in the desired format;
4. Move the scan line with a step size of dX/dY to a new line of KIDs;
5. Repeat until the total number of scans for that coordinate is achieved;
6. Switch to the other coordinate axis and perform the same scanning technique a second time.

Automating the experimental setup this way ensures a consistent and laid-back measurement procedure. Worth noting is the advantage of setting the start and end coordinates of the scan line past the outer edges of the chip. This ensures none of the KIDs are neglected during the scanning procedure.
Another important point to raise is that one must not forget to record the KID array response to a completely blacked out display, which from hereon will be referred to as a "dark" measurement. This is going to serve as the control signal where the KIDs each produce a transmission dip at their characteristic resonance frequency. The signals where the display illuminates a row/column of KIDs, will then be compared to this control signal.

## 5.5 Data Analysis

The goal in the data analysis is to produce a spatial map of the KID array based on the performed measurements. It acts as the main tool to investigate and obtain a measure of the f-scatter in the KID array.

Firstly, the characteristic resonance dips in the dark measurement signal need to be located, which the scipy module `signal.find_peaks` facilitates. Since the detector array is comprised of 400 KIDs, the parameters of this function must be adjusted to approximate the detection of 400 dips as much as possible, abstaining from including dips coming from noise. When the noise contribution in the signal is too overwhelming to accurately detect resonance dips, performing a single-moving average (SMA) may considered. However, this modification can also smooth out the signal to a point where formerly located dips are no longer detectable. Deciding to perform an SMA highly depends on the structure and quality of the multiplexed signal.

Secondly, each of the resonance dips will have to be assigned a coordinate on the KID array based on their recorded response to the x- and y-scans. In order to illustrate this process, the response of a single dip will be looked at for a scan in the x-direction.
The resonance dip number $n$, the $n^{\text{th}}$ dip detected in the dark signal, shifts when their respective KID is illuminated by the scan line. From this shift, the difference in transmission between the illuminated (scanned) and unilluminated (dark) resonance dip $\Delta|S_{21}|$ can be obtained. When the scan line is positioned exactly on the respective KID, the resonance dip will have shifted to a maximum, $\Delta|S_{21}|_{\text{max}}$. Plotting the $\Delta|S_{21}|$-values of this dip for each scanning measurement against the scan line x-coordinates, expressed

in the step size (px), allows the maximum shift of dip $n$ to be localized, yielding the x-coordinate of the resonance dip $n$.
By repeating the exact same process for a scan in the y-direction, dip $n$ receives the y-coordinate of its location according to the scan measurements. Eventually, all the detected resonance dips in the dark signal are given coordinates based on which x- and y-coordinate of the scan line they had the most severe response deviation.

Thirdly, the spatial mapping can be done. Once the coordinate assignment is completed, a matrix may be constructed where each response dip number will occupy the element according to their assigned coordinates. To visualize how the matrix is organized, a meshgrid can be plotted using the `pyplot.meshgrid` function in the matplotlib module. It is important to remember that the matrix created does not have the same dimensions as the KID array itself, rather the dimensions have been decided by the number of scans in x and y. In order to create a meshgrid with the KID array dimensions ($20 \times 20$), the obtained matrix has to be rescaled. This can be done by either writing an algorithm that manages to successfully reorganize the dip locations, or by filling in the elements of the $20 \times 20$ matrix manually. Deciding the most suitable technique depends entirely on the quality of the coordinate assignment and consequently how well structured the dip locations are in the matrix.
Once the obtained spatial map has been scaled, it can be compared with the spatial map of the design to identify the KIDs with swapped $f_0$-values. As more qualitative measures for the f-scatter, a new value for the standard deviation of the fractional frequency deviation $\sigma_{\delta f/f}$, mentioned in section 3.2, may be extracted from this examination. This provides a characteristic value of the f-scatter across the studied KID array, which can be compared with other KID arrays.

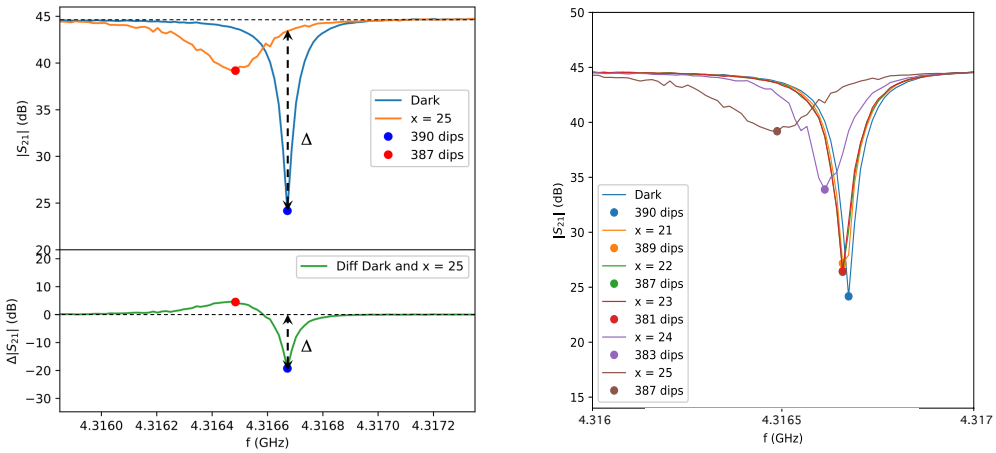


(a) Transmission difference




(b) Dip shift behavior

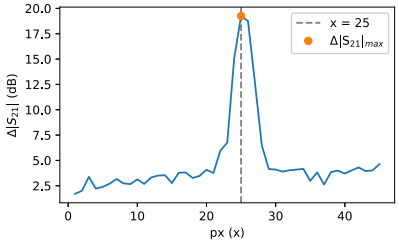


(c) Difference plot x

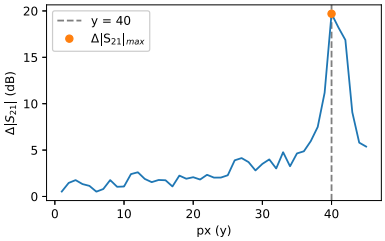


(d) Difference plot y

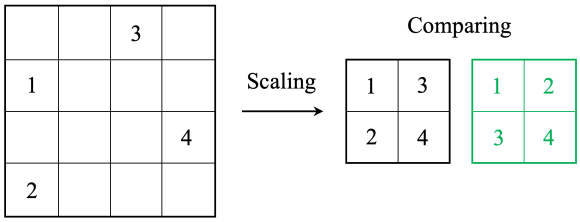


(e) Spatial mapping

Figure 5.4: An overview of the data analysis used in this paper. The data displayed in figures (**a**)-(**d**) are taken from the 49$^{\text{th}}$ dip in the dark signal. Figure (**a**) illustrates how the dip shift can be best approached by looking at the difference $\Delta|S_{21}|$ in transmission amplitude between the dark and illuminated signal. This difference is measured at the $f_0$-location of the dark signal. Figure (**b**) includes the KID response of 6 x-coordinates in one plot in order to display the gradual shift of the resonance dip. The difference across all scans in the x-direction and y-direction (45 per coordinate in this data set) is shown in figure (**c**) and (**d**) respectively. Figure (**e**) displays the construction of a spatial map, based on the coordinates of all detected resonance dips, followed by a simplified illustration of scaling the spatial map to the desired dimensions. This final spatial map can then be compared to the spatial map of the design, illustrated in green. Any differences shall be documented and used to obtain new values for $\phi$ and $\sigma_{\delta f/f}$.

# Chapter 6

# Results

## 6.1 Final Setup

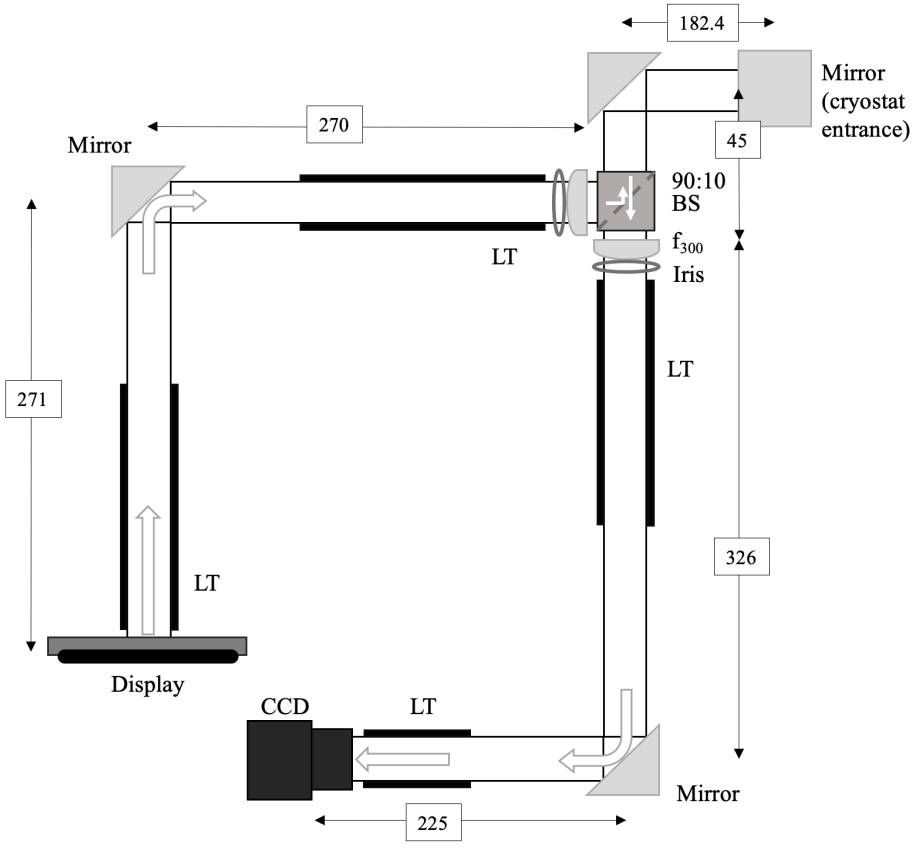


(a) Finalized experimental setup

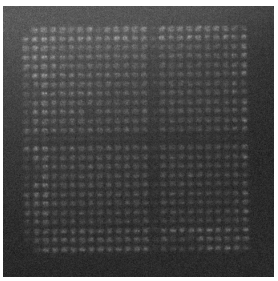

(b) KID array image

Figure 6.1: The aligned experimental setup, used to scan the KID array for inspecting the f-scatter, is illustrated in figure (**a**). The adjusted dimensions are denoted in mm. Figure (**b**) shows an image of the KID array with a horizontal and a vertical scan line imaged on it.

During the alignment procedure of the experimental setup in figure (4.9), the dimensions of the arms have been altered to a total distance of $s_o$ = 541 mm and $s_{i,2}$ = 551 mm, visible in figure (6.1(a)). Given the distance to the KID array chip behind the lens amounts to $s_{i_1}$ = 660.9 mm, the aligned distances provided a magnification of $M_o$ = 1.22 and $M_{i,2}$ = 1.2 respectively. Images of the fully realized setup can be found in Appendix B, along with a list of the used off-the-shelf optomechanical components from Thorlabs®.

## 6.2 Determining Measurement Parameters

With the adjusted setup, an intermediate experiment was conducted in which the measurement parameters were explored for their most suitable settings for the spatial mapping measurements. This includes the display parameters, responsible for the projection of the scan line, and the readout parameters, responsible for capturing the chips response signal. The chosen values, along with the proper motivation, for both parameter sets are listed below.

**Display parameters:**

- `Number of scans = 45`
  - `(x, y)_start = (516px, 1096px)`. The start and end coordinates of the scan line were placed just beyond the outer edges of KID array to make the entire array is scanned. While this does give a number of scans with no illuminated KIDs, this will not impose devastating effects on the other scans.
  - `(x, y)_end = (561px, 1141px)`. Idem ditto.
  - `Step size = 1px`. This step size was chosen to obtain a higher resolution scan, despite the increased duration of the measurement procedure.
- `Color = blue`. As shown by the comparison plot in figure (6.2(a)), the KIDs response to a red and blue scan line (right dip) is stronger than its response to a green line, which can be related to the pixel design of the display. The KIDs response to a white line, however, seemed to be even stronger. While this may be more suitable for a resonance dip shift, the unilluminated KID (left dip) seems to also show a dip shift. This may be attributed to chromatic aberration, described in section 4.3.1.3. For these reasons, the colors blue and red proved to be the best options for a precise spatial mapping measurement. Due to the higher photon energy of the blue colored light, it was ultimately decided to opt for a blue scan line.
- `Line width = 1 px`. The thinnest line width of 1 px matched well the dark signal for an unilluminated KID and showed detectable deviation in $f_0$ for an illuminated KID, see figure (6.2(b)). More importantly, a 1 px wide scan line provides a clearer peak in $\Delta|S_{21}|$, compared to line widths 2 and 3 px. The shallower the peak becomes, the slower the $\Delta|S_{21}|$ seems to change, resulting in a plateau-ing signal around the peak. This can jeopardize the accuracy of the coordinate assignment. For this reason, the line width 1 px was chosen for the scan line on the display.

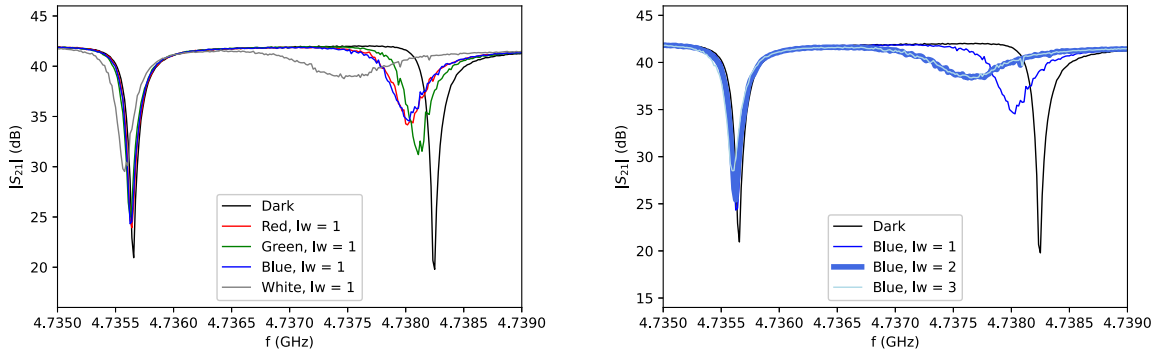


(a) Color (b) Line width, blue

Figure 6.2: Figures (**a**) (**b**) and (**c**) display a plot with various settings for the inversion, color and line width respectively.

**Readout parameters:**

- `Readout Power = -110 dBm`. The readout power $P_{\mathbf{read}}$ was set to -110 dBm for its acceptable SNR for the spatial mapping measurements.
- `Number of points per scan = 12801 points/scan`. Accurately capturing the resonance dips gains priority, as detecting them is the very first and most important step in the spatial mapping data analysis, see figure (6.3(a))
- `Bandwidth per scan = 100 MHz`. Idem ditto, see figure (6.3(b)).
- `IF bandwidth = 1 kHz`. The IF bandwidth was set to 1 kHz in order to smooth out the acquired signal, whilst keep the duration of the measurement procedure at a reasonable length of $\sim$ 3.5 hours, see figure (6.3(c)).

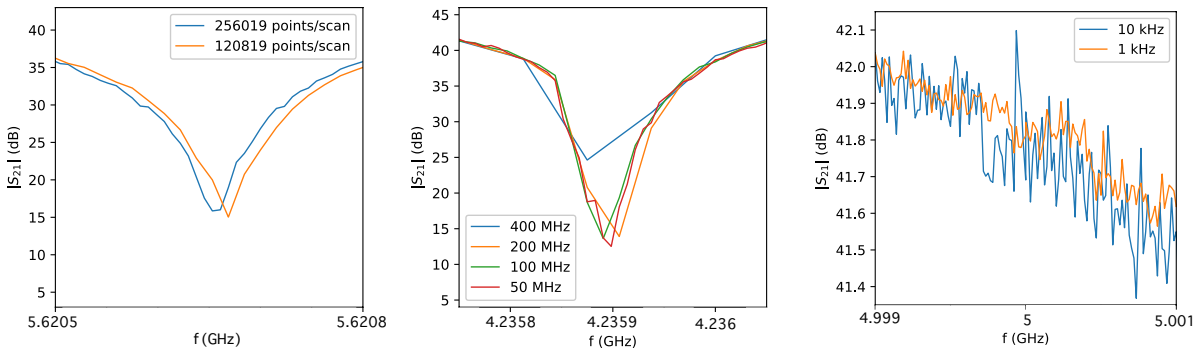


(a) Number of points per scan (b) Bandwidth per scan (c) IF bandwidth

Figure 6.3: Plots displaying a comparison between varying settings of the inversion, colors and line width in (**a**), (**b**) and (**c**) respectively.

## 6.3 Analyzing KID Design

After obtaining the multiplexed KID response in total darkness, the histogram in figure (6.4) was constructed and yielded an average value of $\langle\phi\rangle = 4.18 \pm 0.28$ MHz. In the case of perfect frequency spacing according to the design, one achieves a narrow histogram around $\langle\phi_D\rangle = 4$ MHz, completely separated from $\phi = 0$. This is clearly not the case, which makes it is easy to recognize the likeliness that KIDs have swapped $f_0$, leading to a large amount of f-scatter across the detector array.

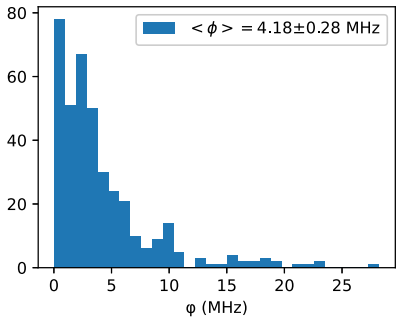


Figure 6.4: A histogram of the frequency spacing $\phi$ across all KIDs on the $20 \times 20$ KID array. The spacing between two consecutive dips is very dispersed across a wide range, instead of narrow as designed. The large gap between the two frequency bands was omitted in the compilation of this histogram.

In order to get a view of the f-scatter across all KIDs, the fractional frequency deviation $\delta f/f$ is plotted in figure (6.5). The standard deviation of the fractional frequency deviation, $\sigma_{\delta f/f} = 5.80 \cdot 10^{-3}$, represents the f-scatter as an intrinsic value for the KID array. However, this value is of the $\delta f/f$ before spatial mapping, which makes it inaccurate. Nonetheless, the obtained $\delta f/f$ plot provides several important points that deserve to be raised:

1. The entire KID detector exhibits a negative $\delta f/f$. This is due to the fact that the resonance frequencies were designed to range from around 4.5 to 6.5 GHz, but measurements point out the range has shifted to around 4 to 6 GHz.

2. Despite the expected amount of detected resonance dips is 400, only 390 KIDs were detected by the `signal.find_peaks` function, which means there are 10 KID responses missing. Since the missing dips can not be localized by simply looking at the design, there is a indeterminable shift $f_0$ per KID number. This is best reflected in sudden decrease in negative $\delta f/f$. The only area that discloses some information about the location of the missing dips, is around the KID number 200. From the behavior of $\delta f/f$ here, the dip detection can be stated to have "skipped" 6 resonance dips in the first frequency band and 4 in the second. This explains an earlier jump to the second higher frequency band, illustrated in figure (6.5). Due to this jump, these 6 outlying point have been omitted from the determination of $\sigma_{\delta f/f}$.

3. There seems to be a positive trend in $\delta f/f$ plotted against the KID number. The fractional deviation from the designed resonance frequency seems to be smaller for higher KID numbers (KIDs with higher $f_0$) than it is for the lower KID numbers (KIDs with lower $f_0$).

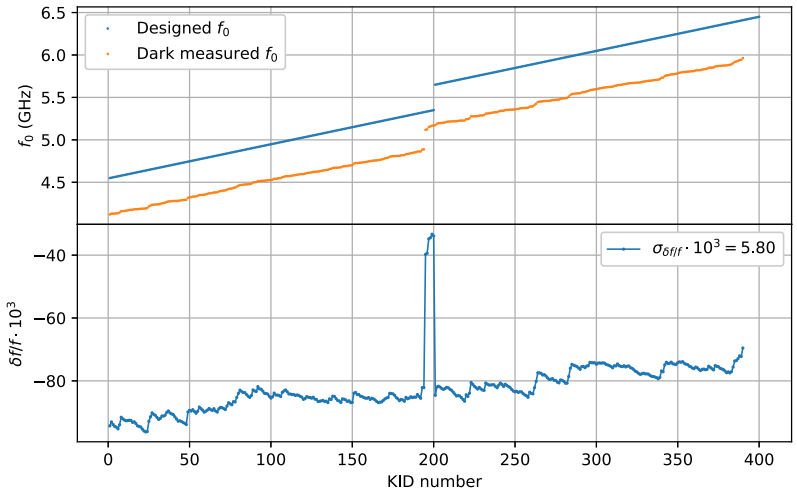


Figure 6.5: The dark measured and designed resonance frequencies plotted together (top) and the fractional frequency deviation of the measured $f_0$ to the designed $f_0$ according to equation (3.1). There is a systematic shift of the measured $f_0$ of $\sim$ 0.5 GHz, which does not gravely impact the $\delta f/f$ as it is an near stationary plot. However, visible is the measured $f_0$ making a jump to the second frequency band at an earlier KID number than the designed $f_0$. This means that there were a number of KIDs before the 200$^{\text{th}}$ KID that have not been detected in the data analysis.

## 6.4 $45 \times 45$ Spatial Map

The combination of the aligned experimental setup, the optimal parameters applied to the measurement procedure and the provided data analysis, produced a spatial map of the KID array displayed in figure (6.6). The aforementioned 10 missing dips are leaving obvious empty pixels in this spacial map. However, when studying the amount of pixels on the spatial map, it has decreased from 390 to 385 pixels. The root cause of the 10 initially missing dips and the additional 5 dips will be explored in this section.

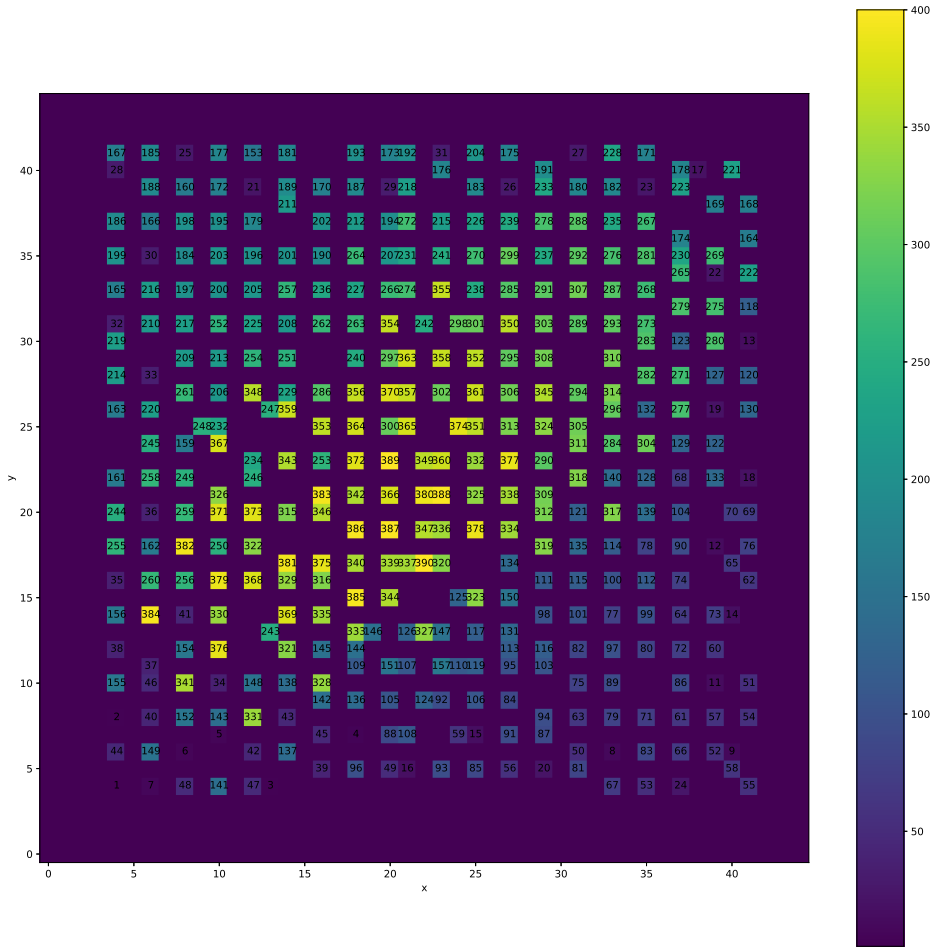


Figure 6.6: A $45 \times 45$ spatial map of the detector array based on the scanning measurements. Due to the small step size of the scan line, the pixels are nearly evenly spaced, which makes the detector array design more recognizable. However, this even spacing is disturbed around the center because the step size does not match exactly with the KID arrangement on the detector array. The empty pixel spaces in this map amount to a total of 15, since there are only 385 pixels instead of the expected 400.

### 6.4.1 Overlapping Dips in Dark Signal

The first cause of missing pixels in the $45 \times 45$ spatial map goes back to the obtained KID signal and how the coordinate identification is executed. The frequency spacing histogram in figure (6.4) shows $\phi$ values close to zero, which sparks the suspicion there are dips that overlap each other, $\phi \approx 0$. If this were the case, then the single dip in the dark signal would have a deviating response for two separate scan line coordinates,

leading to two peaks in the dips $\Delta|S_{21}|$ plot. In total, four of these overlapping dips have been detected, listed in table 6.1. The $\Delta|S_{21}|$ plots of the overlapping dips are visible in Appendix C for inspection.

Table 6.1: The four dips that have been discovered to be made up of two overlapping dips. The dips are organized according to the scan direction in which the dips have been discovered. The fact that the dips match almost perfectly shows that both scans in the x- and y-direction have been able to identify the same overlapping dips, hinting at the accuracy of these findings.

| Dip in the x scan | Dip in the y scan |
|---|---|
| 70 | 70 |
| 164 | 164 |
| 332 | 332 |
| 354 | 353 |

Since the location of these overwritten can be determined, they can be included in the $45 \times 45$ spatial map, where the manage to fill up prevalent empty pixel spaces. However, figure (6.7) shows that the behavior of an overlapped dip is too inconsistent to assign a $f_0$ value to each of the individual dips. For this reason, these pixels are excluded from the comparison steps of the data analysis.

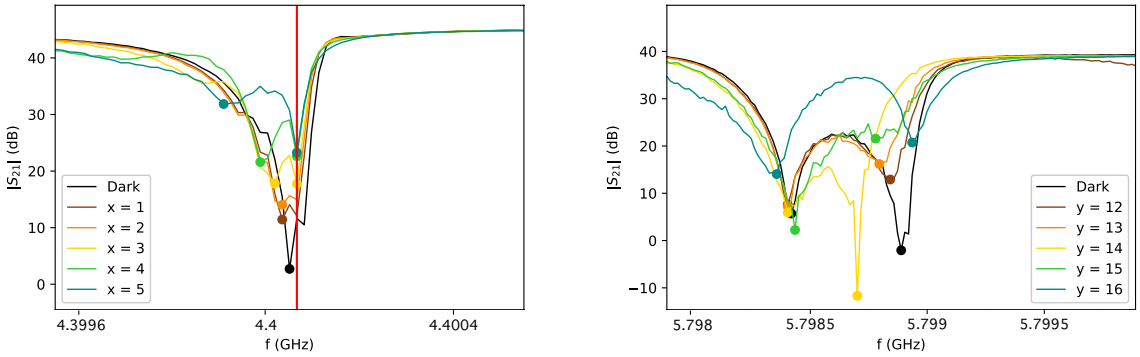


(a) Dip 70, $x_{\mathbf{max}} = 5$

(b) Dip 353, $x_{\mathbf{max}} = 16$

Figure 6.7: The comparison plots of two dips consisting of two overlapping dips. The dips were plotted in varying coordinates to show how the respective KID illumination causes one of the dips to shift, giving away a glimpse the two individual dips as in figure (**a**). However, this behavior is not consistent, as figure (**b**) shows.

### 6.4.2 Overwriting Dips on Spatial Mapping

Unlike in the case of the overlapping dips, the coordinate identification and the meshgrid creation can be held accountable for the second cause of missing pixels in the $45 \times 45$ spatial map. When it comes down to assembling the spatial map, the pixel occupied by the first dip will be overwritten by the second dip, leading to a doubly occupied pixel. These "first" dips can be recovered and are included in table (6.2).

Table 6.2: The five dips that have been lost during the assembly of the spatial map. The dips listed below the header "First dip" have been overwritten by the dips listed below "Second dip".

| First dip | Second dip | Shared spatial map coordinates |
|---|---|---|
| 10 | 164 | (41,36) |
| 102 | 117 | (25,13) |
| 362 | 363 | (21,29) |
| 158 | 344 | (20,15) |
| 224 | 225 | (12,31) |

During the coordinate identification, two dips may be assigned the same coordinates according to the $\Delta|S_{21}|$ plot. This is done based on which scan coordinates yield the peak value. However, the plot of $\Delta|S_{21}|$ uses a limited amount of points, fixing the resolution of the signal. This means that in the area around the maximum value, the accuracy with which the real maximum value is determined, is also limited.
An additional cause of wrong coordinate assignment is the imperfection reflected in the detector responses. Visible in the plot for dip number 117, figure (6.8(b)), is a plateauing $\Delta|S_{21}|$, which allows the algorithm to "choose" a coordinate rather than determining it, leading to a possibly faulty coordinate prescription.

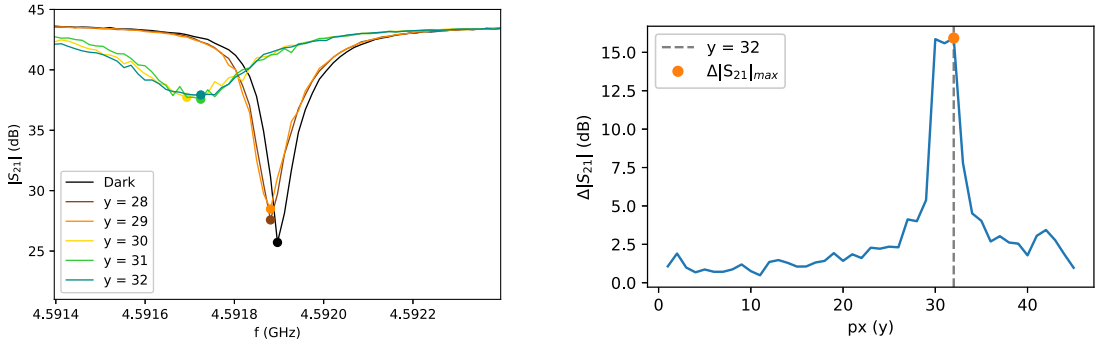


(a) Signal of dip 117 for 5 y-coordinate scans

(b) Transmission difference plot of dip 117

Figure 6.8: Figure (**a**) shows the gradual behavior of the transmission signal of dip 117 with the progressing y-coordinate scan. At scan $y = 30$, the signal maintains the same position for three consecutive scans, which is reflected in the plateauing signal around the peak in figure (**b**).

Since these dips can be recovered, they can be assigned a new coordinate based on the provided $20 \times 20$ KID array design. However, this reassignment can not always be done with complete certainty, particularly in areas where the pixel spacing is very chaotic. For this reason, these pixels too are excluded from the comparison steps of the data analysis.

## 6.5 $20 \times 20$ Spatial Map

### 6.5.1 Scaling Procedure

The scaling of the $45 \times 45$ spatial map to a $20 \times 20$ spatial map was performed manually, see the right spatial map in figure (6.9). As a result, any pixels of which their coordinates on the $20 \times 20$ spatial map could not be determined with certainty, were excluded, leaving a gaping hole in the center of the spatial map. The resulting pixel yield has further decreased from 385 to 374 pixels. The findings presented at the end of

this section, will therefore disregard the presence of 26 KIDs that have not been carried through the data analysis, making up 6.5% of the total amount of KIDs.

### 6.5.2 Comparison with Design

In the direct comparison of the obtained measurement spatial map with the provided design spatial map of the KID array, there seem to be only 22 KIDs that have not swapped their $f_0$ with other KIDs, see figure (6.9). Thus there are 378 pixels on the measured spatial map with a significant $f_0$ shift.

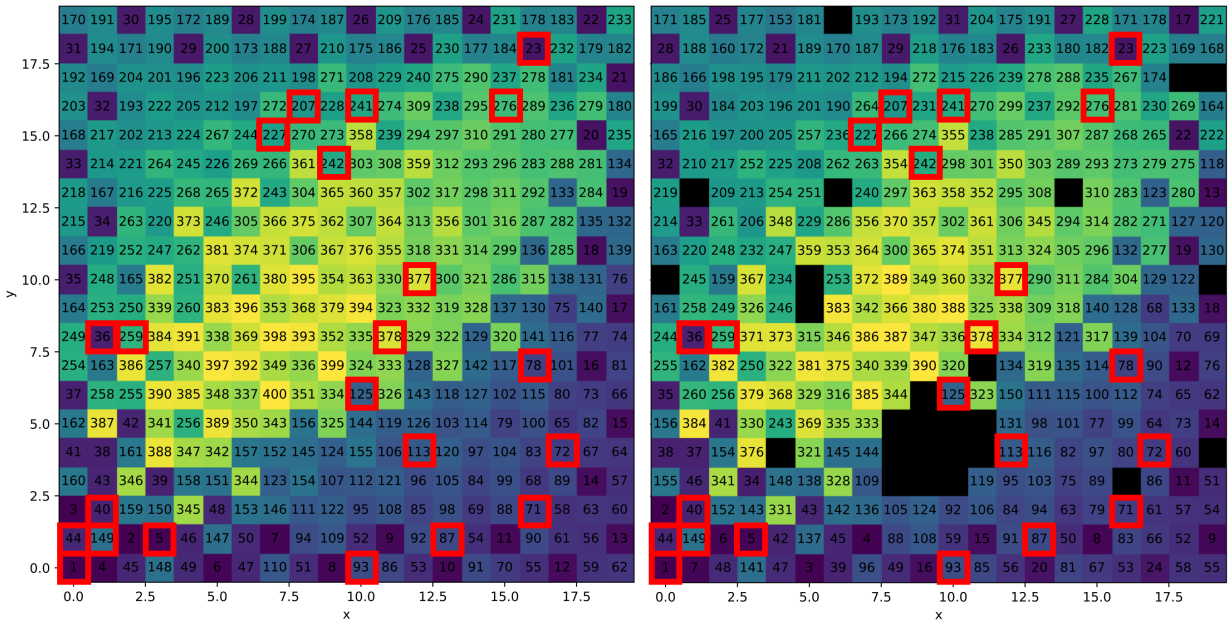


Figure 6.9: A comparison of the designed KID array spatial map (left) and the obtained KID array spatial map through measurements (right). The pixels contained by a red box represent the KIDs that have kept their designated $f_0$-value after fabrication. In the light of needing precise values for the comparison with the designed spatial map, pixels accompanied by too much location uncertainty were omitted in this spatial map. Hence, the pixel yield has become 374 instead of the expected 400.

The large amount of KIDs with shifted $f_0$ ultimately re-engineers the frequency spacing between two consecutive dips in the dark signal. Instead of simply taking $\delta f/f$ between two consecutive detected dips, the algorithm can now recognize which dip belongs to which KID and order resonance dips on the dark signal accordingly. The newly obtained $\phi$-distribution, see figure (6.11), becomes much more dispersed and has negative frequency spacing. This is a consequence of resonance dips having such a large f-scatter that they appear before the precedent resonance dip, $f_{n+1} < f_n$, instead of after, $f_{n+1} > f_n$. This is referred to as the swapping of $f_0$-values between two KIDs.

In order to get a good impression of the severity of the f-scatter in this $20 \times 20$ KID array is, the fractional frequency deviation $\delta f/f$ needs to be studied. The comparison of the KID array before and after spatial mapping are presented in figures (6.11) (6.12). From the updated distribution, a new value for the standard deviation could be obtained, $\sigma_{\delta f/f} = 5.92 \cdot 10^{-3}$. A few things can be said about this value and the presented histograms:

- The $\delta f/f$ distribution before applying spatial mapping has a different shape than that of the $\delta f/f$ distribution after. The former has two very apparent peaks and is fairly smoothed out in their nearby

surroundings. The latter displays more of a plateau, indicating there is a more uniform f-scatter in the KID array than previously assumed. The observation that the "after" distributions is not dispersed more widely than the "before" distribution, explains why $\sigma_{\delta f/f,\text{after}}$ ($= 5.92 \cdot 10^{-3}$) is quite close to $\sigma_{\delta f/f,\text{before}}$ ($= 5.80 \cdot 10^{-3}$).

- The $\delta f/f$ distribution after spatial mapping seems to have sifted towards larger negative values. This is reflected in the distribution mean $\mu_{\delta f/f,\text{after}} = -86.7 \cdot 10^{-3}$, while $\mu_{\delta f/f,\text{before}} = -83.0 \cdot 10^{-3}$.

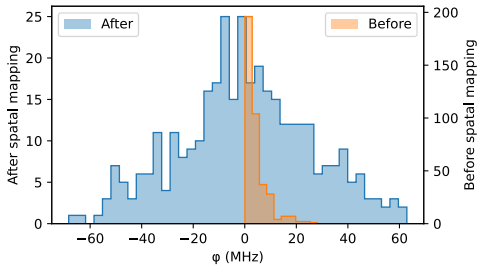


Figure 6.10: A histogram in which the frequency spacing of the resonance dips $\phi$ are compared before and after performing spatial mapping. This comparison illustrates the true scale of the f-scatter in the fabricated KID array. The "before" is entirely positive, while the "after" has negative $\phi$. This is due to KIDs with higher designed $f_0$ taking on a much lower $f_0$ in during the measurements. Such a resonance dip is then shifted to before the precedent resonance dip: $f_{n+1} < f_n \rightarrow \phi < 0$.

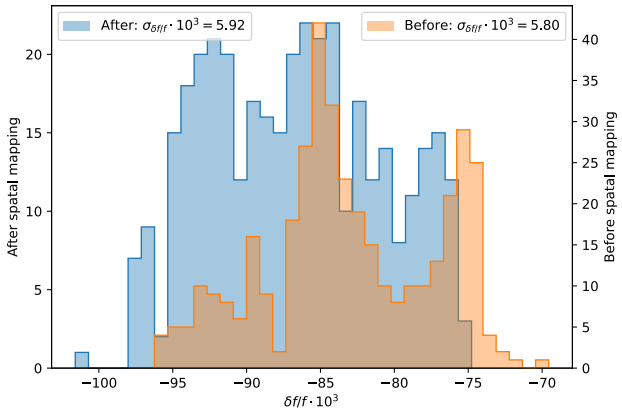


Figure 6.11: The comparison of the fractional frequency deviation $\delta f/f$ distributions before and after performing spatial mapping. The "before" and "after" distributions mainly differ in shape rather than in dispersion, which is reflected in the standard deviation being quite similar, $\sigma_{\delta f/f} = 5.80 \cdot 10^{-3}$ and $\sigma_{\delta f/f} = 5.92 \cdot 10^{-3}$ respectively. The "after" distribution does display a slight shift towards a more negative $\mu_{\delta f/f}$. This implies that the spatial mapping technique was able to recognize a larger systemic fractional frequency deviation.

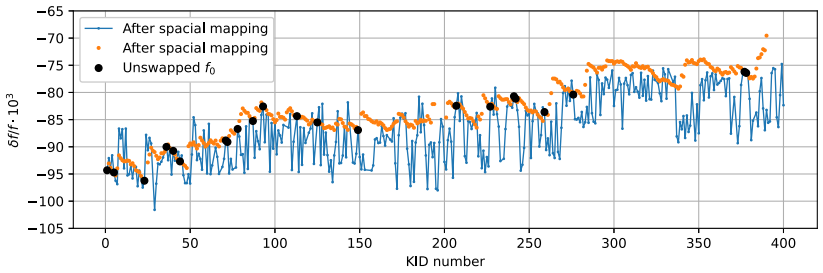


Figure 6.12: The comparison of the fractional frequency deviation $\delta f/f$ plots. This plot provides a visualisation of the $\delta f/f$ difference of each individual KID between before and after applying spatial mapping. The "before" reaches at KID number 390, due to the fact the dip detection was able to reveal only 390 resonance dips. Because the spatial mapping is able to re-assign KID numbers new $f_0$-values, the "after" plot reaches KID number 400. However, this plot consists of only 374 points, which represents total number of resonance dips that made it onto the the $20 \times 20$ spatial map. Of these 374 KIDs, 22 KIDs have been determined to have unchanged or unswapped $f_0$-values compared to the design, which are marked black. Something also quite remarkable, is that the trend in the "before" plot seems to be slightly more positive than that of the "after" plot.

# Chapter 7

# Conclusions & Discussions

This chapter presents a recapitulation of all the developments discussed in this paper, as well as a thorough evaluation of the viability of the finalized experimental method with prospects for future research.

## 7.1 Summary and Conclusion

The goal of this paper was to design an experimental method that could be used to investigate the frequency scatter in an optical KID array. The principle of the experimental method is performing a scan of the KID array in the x- and y-direction to produce a spatial map of the KID array, which is compared to the original design to inspect the f-scatter. Bringing the presented method to realization consisted of three key components: designing and constructing the experimental setup, developing a sufficient measurement procedure, and building a functioning data analysis architecture that can be used to interpret the measurements obtained with the setup. The outcome and findings from each of these components are presented in this section.

Firstly, an optical setup was designed, based on several criteria set to optimize the quality of measurements. The constructed setup is capable of imaging a scan line, projected onto an AMOLED display, onto the KID array chip inside a cryostat. The optical system implemented is a two-armed single-lens system with negligible contributions from field curvature and distortion. One arm is reserved for the display with a magnification of $M = -1.22$ and the other for a CCD camera to facilitate alignment ($M = -1.20$). In total, the components responsible for alignment provided six degrees of freedom in the optical setup.
Secondly, the readout system and the display were synchronized and automated to make sure the scanning could be executed with no obstructions introduced by human intervention. The settings of the scan line were decided based on how well the KIDs responded to illumination, compared to a dark measurement. The readout settings were decided based on which provided a high SNR and accurate dip capturing.
Thirdly, the measurement procedure was executed using the constructed optical setup and produced a $45 \times 45$ spatial map. After scaling the spatial map to $20 \times 20$, the pixel yield was reduced from 400 to 374 due to undetected dips, overlapping dips, overwritten pixels and uncertainty in pixel location. Despite this, comparing the obtained spatial map with the provided design provided a clear illustration of the true frequency spacing $\phi$ across the fabricated KID array. The spatial map comparison also delivered the true value for the standard deviation of the fractional frequency deviation of $\sigma_{\delta f/f} = 5.92 \cdot 10^{-3}$. This is a property intrinsic to the fabricated KID array, as it is a measure of the severity of the f-scatter across the KID array. It can therefore be used when comparing fabricated KID arrays based on how well they match their design.

In conclusion, the experimental method presented above was able to provide useful information about the f-scatter of the $20 \times 20$ KID array. However, this method only managed to incorporate 93.5% of all KIDs on the detector array. The next section evaluates various components of the developed experimental method and provides recommendations to improve it.

## 7.2 Evaluation and Prospects

### Lens Systems

The magnification of the current optical setup is constrained to a limited value, as the optical system is a single-lens system. Achieving smaller magnifications is favorable because it allows more precise scanning of the detector array. Settings, such as the line width and scan line step size, can be changed more freely, which are largely constrained by the $M$ of the single-lens system.
One such system is the two-lens system utilizing the principle of virtual imaging, already discussed in section 4.2.2.2. The benefits of this system is it provides the opportunity to image with $|M| < 1$ without increasing $s_o$ beyond the workspace area limits. Suggested is a better understanding of the design and construction of this system and, eventually, how it can be optimized to serve the purpose of this experiment.
Another system that is especially advantageous with regards to eliminating aberrations, is the Cooke triplet. This system uses three lenses which are able correct each others optical aberrations. Therefore, it has the potential to produce a scan line image on the chip with a very high resolution and with more concentrated power. This allows for more control on which KIDs are illuminated and which are not, resulting in more prevalent KID responses that are better detectable. This could also form the solution to one of the biggest flaws of the developed data analysis, which is its inability to detect all resonance dips of the 400 KIDs.

### Improved Alignment Process

While the six degrees of freedom of the current setup allows for proper alignment, it is still arduous to complete. The biggest struggle can be found in the z-rotation, which is the orientation of the optical able with respect to the chip inside the cryostat. Because the optical table is quite heavy, and the slightest of rotations have large effect on the alignment of the setup, rotating it into the correct orientation is not easy and can take a long time. Therefore, another alignment measure that takes care of the optical setup orientation is desired.
A possible solution would be a firm structure providing direct connection between the optical table and the outer shell of the cryostat. When the orientation of the setup needs to be adjusted, the structure will allow the setup to be rotated, whilst making sure the kinematic mirror stays below the cryostat. This is a more mechanical approach to solving this problem. However, any solution involving geometrical optics would be even better, as moving the optical table is preferred to be minimized.

### Scanning Techniques

The scanning technique used in this paper, moving a straight line across the x- and y-axis of the KID array, is effective but it takes a long time as it requires a large number of scans. In the case that lens systems are able to image the display with $|M| < 1$ and high resolution, other scanning techniques may be explored. Examples of new convenient scanning techniques would be:

- Fractal scanning. The principle of this technique is by dividing the detector array into sections and scanning them according to how it has been sectioned. These sections can then be divided into smaller sections and scanned. Doing this until single KIDs are scanned provides each KID with a unique scan sequence. This way, the number of scans per measurement can be significantly reduced.
- Scanning using QR codes. Lets say a QR code is imaged on a $20 \times 20$ KID array. Each KID can then respond in a binary fashion. For this detector it would only take 9 scans ($2^9 = 512$) to give each KID a unique binary code. This makes it easily recognizable in coordinate identification.

### Overwritten Dips

A pronounced flaw of the data analysis developed in this paper, is a botched coordinate identification process. While the setup and scanning technique do contribute to this, it is not wrong to look at how the

present noise impacts the quality of this process. Section 6.4.2 touched on overwritten pixels on the spatial map as a result of the imperfect coordinate assignment. When the detectors deviated resonance dip is stationary for multiple scans, the presence of noise has a large effect on the determination of $\Delta|S_{21}|_{\max}$. This forces the algorithm to detect it based on noise and not on the actual measurement, which could lead to a faulty outcome.
A possible solution is increasing the SNR by reducing the IF bandwidth. When deciding this, one must take into account the increased duration of a single scan. Otherwise, applying a simple moving average during the data analysis could significantly smooth out the signal, although this must never be at the expense of dip detection.

### Overlapping Dips

Section 6.4.1 showed that dips that overlap with each other were identifiable despite the quality of the signal. However, the behavior of overlapping dips is simply too inconsistent to formulate a behavioral pattern, especially with regards to finding the $f_0$ of the individual dips. Including both distinguishable dips can therefore only be done when the determination of the $f_0$-values of each dip is viable and reliable. It is thus recommended to conduct more research on the behavior of overlapping dips.

# Bibliography


[1] W. Ras, "Microwave Kinetic Inductance Detectors For The Mid-Infrared," Master's thesis, Delft University of Technology, Delft, Nov. 2022.

[2] J. Baselmans, "Kinetic Inductance Detectors," *Journal of Low Temperature Physics*, vol. 167, pp. 292–304, May 2012.

[3] D.-Y. Chung, "The basic cause of superconductivity," *Journal of Modern Physics*, vol. 06, pp. 26–36, 01 2015.

[4] E. Vaal, *Validity of analytical Microwave Kinetic Inductance Detector responsivity expressions*. Bachelor Thesis, Delft University of Technology, Delft, July 2016.

[5] N. Vercruyssen, R. Barends, T. M. Klapwijk, J. T. Muhonen, M. Meschke, and J. P. Pekola, "Substrate-dependent quasiparticle recombination time in superconducting resonators," *Applied Physics Letters*, vol. 99, p. 062509, Aug. 2011.

[6] J. Gao, J. Zmuidzinas, A. Vayonakis, P. Day, B. Mazin, and H. Leduc, "Equivalence of the Effects on the Complex Conductivity of Superconductor due to Temperature Change and External Pair Breaking," *Journal of Low Temperature Physics*, vol. 151, pp. 557–563, Apr. 2008.

[7] B. A. Mazin, "Microwave Kinetic Inductance Detectors," Master's thesis, California Institute of Technology, Pasadena, Aug. 2004.

[8] N. Storey, *Electronics: A Systems Approach*. Pearson, 6 ed., 2017.

[9] K. Kouwenhoven, D. Fan, E. Biancalani, S. A. de Rooij, T. Karim, C. S. Smith, V. Murugesan, D. J. Thoen, J. J. Baselmans, and P. J. de Visser, "Resolving power of visible-to-near-infrared hybrid $\beta-$Ta/Nb$-$Ti$-$N kinetic inductance detectors," *Phys. Rev. Appl.*, vol. 19, p. 034007, Mar 2023.

[10] N. Bhoedjang, *Evaluating Frequency Scatter in Optical Kinetic Inductance Detector Arrays*. Bachelor Thesis, Delft University of Technology, Delft, 2023.

[11] S. Verheul, "Ultra High Sensitivity Microwave Kinetic Inductance Detectors," Master's thesis, Delft University of Technology, Delft, July 2019.

[12] P. J. De Visser, *Quasiparticle dynamics in aluminium superconducting microwave resonators*. Doctoral, Delft University of Technology, Delft, 2014.

[13] E. Hecht, *Optics, International Edition*. San Fransisco, CA: Pearson Education, Inc., 4 ed., 2002.

[14] A. Adam, S. Konijnenburg, and P. Urbach, *BSc Optics*. Delft: TU Delft Open, 2nd ed., 2022.

[15] Wikipedia, "Circle of confusion," Nov. 2022. Page Version ID: 1122022692.

[16] J. Pradhan, N. Das, and A. Chakrabarti, "Transient phenomena initiating phase transition in dilution refrigerator," *Cryogenics*, vol. 63, 09 2014.

[17] Michael Bottom, Leo S. Neat, Leon K. Harding, Patrick Morrissey, Seth R. Meeker, and Richard T. Demers, "Smartphone scene generator for efficient characterization of visible imaging detectors," July 2018.

[18] Elevise, "Electromagnetic spectrum," 2016.

# Appendix A

## Electromagnetic Spectrum

The electromagnetic (EM) spectrum is a spectrum that contains a range of electromagnetic radiation based on their wavelength $\lambda$, frequency $f$ and energy $E$. [14] An illustration of this spectrum is provided in figure (A.1).

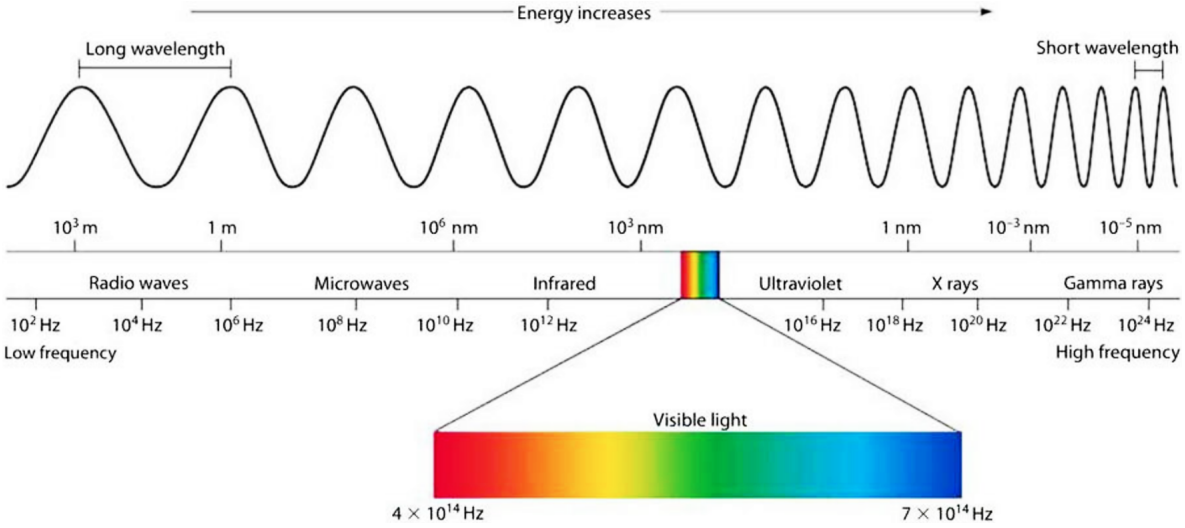


Figure A.1: The electromagnetic spectrum. The visible light region is defined in terms of frequency, which is inversely proportional to the wavelength, $f \sim \lambda^{-1}$. As red light has a frequency of $4 \cdot 10^{14}$ Hz and blue light has a frequency of $7 \cdot 10^{14}$ Hz, they have a wavelength of 700 nm and 400 nm respectively. [18]

# Appendix B

This part of the Appendix focuses entirely on the optical setup. Table (A.1) presents a list all the optomechanical components used to construct the finalized setup. Images of this setup are available in figures (B.1(a-e)).

## Thorlabs® Equipment

Table A.1: A list of all the off-the-sheld optomechanical components from Thorlabs® that make up the entire construction the optical setup used in this paper.

| **Component** | **Part Number** | **Quantity** | **Subtotal (€)** |
|---|---|---|---|
| 90:10 (R:T) Beamsplitter Cube | BS028 | 1 | 224,44 |
| Kinematic Cage Cube Insert for Beamsplitter Cubes | DFM1T5 | 1 | 267,25 |
| Cage Cube-Mounted Right Angle Mirror | CCM1-G01/M | 2 | 346,94 |
| Kinematic Cage Cube Base | DFM1B | 1 | 155,69 |
| Kinematic Cage Cube Insert | DFM1T4 | 1 | 264,66 |
| Cage Cube Connector | CM1-CC | 1 | 47,65 |
| Right-Angle Kinematic Mirror Mount | KCB1/M | 1 | 140,58 |
| Broadband Dielectric Mirror | BB1-E02 | 1 | 73,83 |
| Achromatic Doublet (f=300 mm) | AC254-300-A-ML | 2 | 207,50 |
| Iris Diaphragm (Ø0.8 - Ø20 mm) | CP20D | 2 | 185,90 |
| Threaded 30 mm Cage Plate, (diameter = 1") | CP33/M | 10 | 173,50 |
| Cage Plate, (diameter = 1.2") | CP36 | 4 | 86,36 |
| Cage Plate Connector | SM1T4 | 2 | 52,84 |
| 6" Lens Tube | SM1E60 | 3 | 142,95 |
| 2" Cage Assembly Rod (4 Pack) | ER2-P4 | 1 | 22,79 |
| 6" Cage Assembly Rod (4 Pack) | ER6-P4 | 3 | 96,93 |
| 10" Cage Assembly Rod | ER10 | 8 | 99,84 |
| Rod Adapter (length = 0.27") (4 Pack) | ERSCB | 3 | 171,81 |
| Optical Post (length = 40 mm) | TR40/M | 6 | 32,16 |
| Post Holder (length = 20 mm) | PH20/M | 4 | 29,72 |
| Pedestal Base Adapter | BE1/M | 4 | 39,36 |
| Clamping Forks | CF125C | 4 | 45,76 |
| Mounting Base | BA2/M | 2 | 14,72 |
| | | | **2923,18** |

The optical setup that was used in this paper, was constructed of off-the-shelf optomechanical components from Thorlabs®. The fact that they were off-the-shelf made them readily available to be ordered and delivered. A complete list of all the implemented components is provided in table (A.1).

The display and the CCD camera that were implemented into the setup, were not included in this list, as they are not sold by Thorlabs®. The OnePlus 6T smartphone, of which the display was used for performing measurements, was self-purchased. The CCD-camera was already available at the facility where the experiment was conducted.

## Images of the Constructed Setup

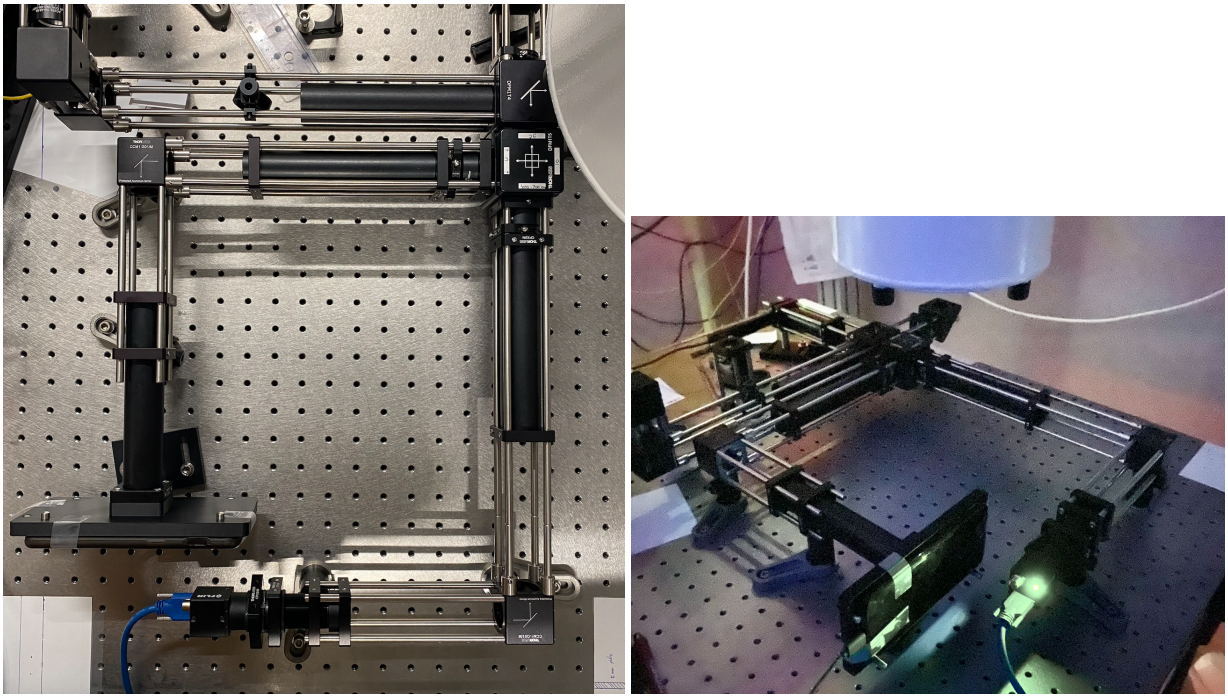

(a) Top view (b) While performing measurements

Figure B.1: (**a**) The top view of the entire optical system, constructed to match up with the design sketches. (**b**) An image capturing the setup in middle of performing measurements, hence the dark environment.

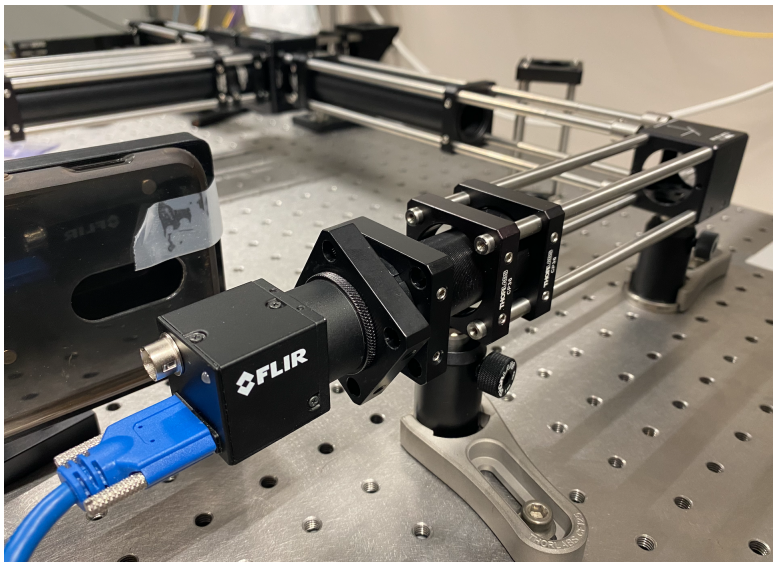


(c) CCD Camera

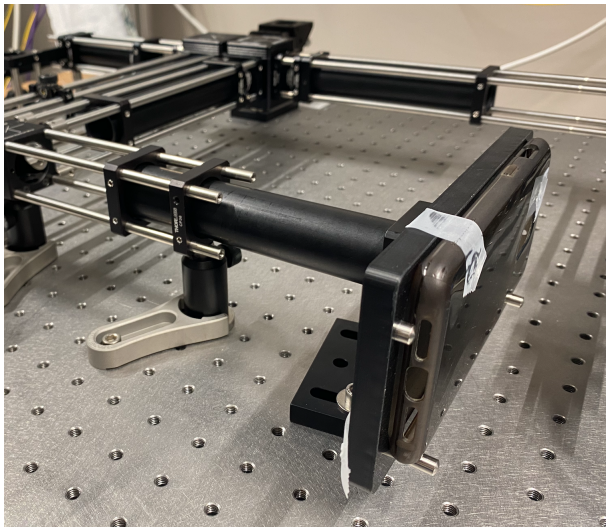

(d) 3D printed display holder

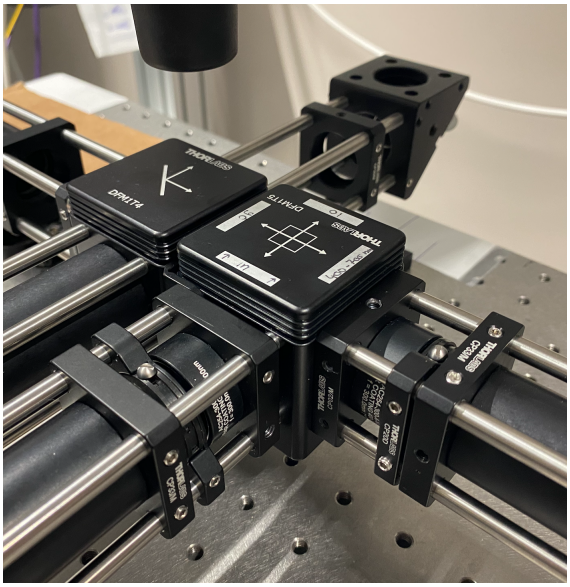

(e) Closeup near the cryostat entrance

Figure B.1: (**c**) A closeup of the CCD camera mounting mechanism. (**d**) A closeup of the display mounting mechanism, with the 3D printed display holder in the foreground. These two mechanisms allow for adjustable arm length, which is exploited during the alignment procedure. (**e**) A closeup of the optomechanical components near the cryostat entrance. These components are responsible for directing the light from the display to the KID array chip, and for directing the light from the KID array to the CCD camera.

# Appendix C

While investigating the reduced pixel yield, several resonance dips were detected to have been overlapping with a nearby resonance dip. These overlapped dips were detected as one, while they consisted of two. These plots were detected and listed in table (6.1). The overlapping was discovered through the detection of two peaks in the $\Delta|S_{21}|$ plots of each of the overlapped dips, which are displayed in figures (C.1-4).

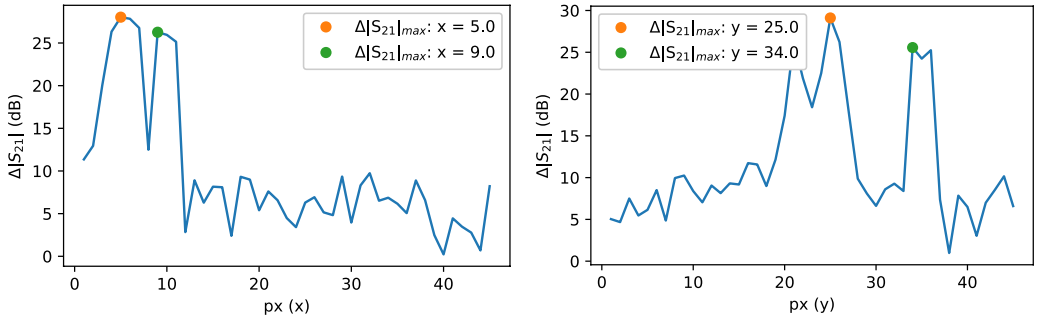


Figure C.1: The $\Delta|S_{21}|$ plots of resonance dip number 70, where two peaks have been identified. These plots capture its response to scans along the x-axis (left) and along the y-axis (right).

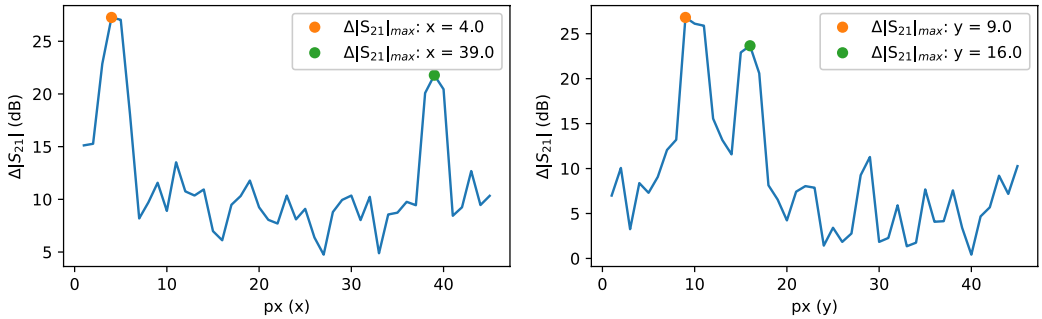


Figure C.2: The $\Delta|S_{21}|$ plots of resonance dip number 164, where two peaks have been identified. These plots capture its response to scans along the x-axis (left) and along the y-axis (right).

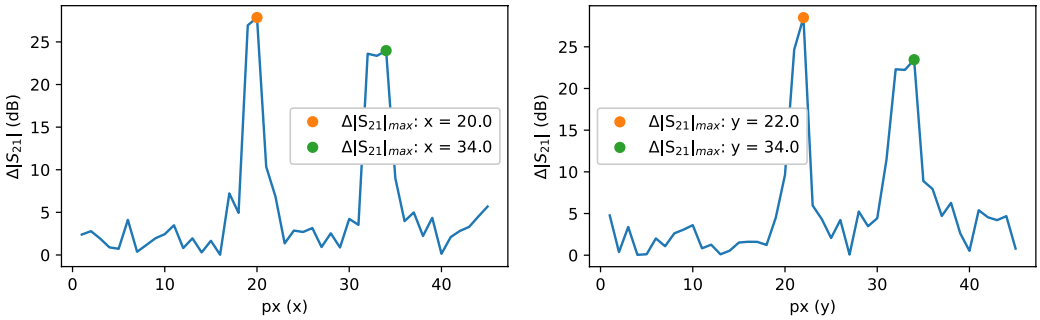


Figure C.3: The $\Delta|S_{21}|$ plots of resonance dip number 332, where two peaks have been identified. These plots capture its response to scans along the x-axis (left) and along the y-axis (right).

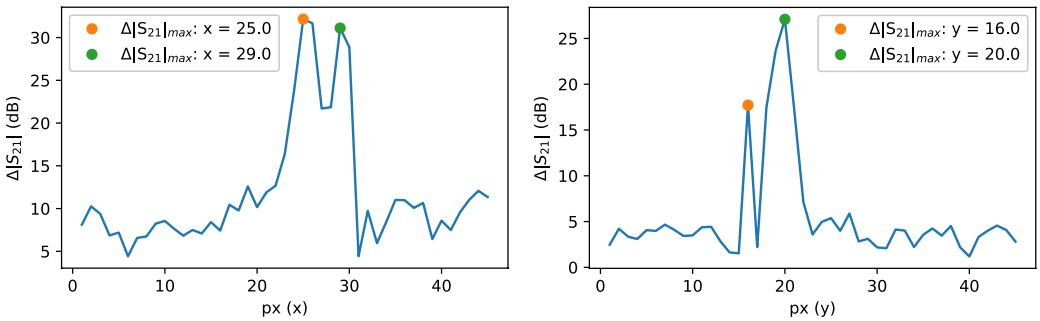


Figure C.4: The $\Delta|S_{21}|$ plots of two separate resonance dips. Two peaks have been identified in the response of dip number 354 to a scan along the x-axis (left). Similarly, two peaks have been identified in the response of dip number 353 to a scan along the y-axis (right).